



## Magnetic biosensors: Modelling and simulation

Vahid Nabaei<sup>a</sup>, Rona Chandrawati<sup>b</sup>, Hadi Heidari<sup>a,\*</sup>

<sup>a</sup> Microelectronics Lab, School of Engineering, University of Glasgow, Glasgow G12 8QQ, UK

<sup>b</sup> School of Chemical and Biomolecular Engineering, The University of Sydney, Sydney, NSW 2006, Australia



### ARTICLE INFO

#### Keywords:

Magnetic sensors  
Modelling  
Simulation  
Hall sensors  
Giant magnetoresistors

### ABSTRACT

In the past few years, magnetoelectronics has emerged as a promising new platform technology in various biosensors for detection, identification, localisation and manipulation of a wide spectrum of biological, physical and chemical agents. The methods are based on the exposure of the magnetic field of a magnetically labelled biomolecule interacting with a complementary biomolecule bound to a magnetic field sensor. This Review presents various schemes of magnetic biosensor techniques from both simulation and modelling as well as analytical and numerical analysis points of view, and the performance variations under magnetic fields at steady and nonstationary states. This is followed by magnetic sensors modelling and simulations using advanced Multiphysics modelling software (e.g. Finite Element Method (FEM) etc.) and home-made developed tools. Furthermore, outlook and future directions of modelling and simulations of magnetic biosensors in different technologies and materials are critically discussed.

### 1. Introduction

In recent years, an enormous surge of works has been carried out to develop new methods for detection of a wide range of biomolecular targets in life-science applications, medical diagnostics, and pharmaceutical discovery. Development of high-speed, reliable, accurate and high-resolution biosensing platforms continues to be driven by the huge market potential for bio-detection systems (Blohm and Guiseppi-Elie, 2001; Chin et al., 2007; Enserink, 2001; Prinz, 1998). Recent research works focusing on magnetic sensors and nanoparticles with applications in biomedicine and their detection by magnetic sensors underpin these efforts. For example, magnetic nanoparticle based hyperthermia treatment, guided drug delivery and the use of magnetic particles as MRI contrast agents are examples of highly successful research and clinical methods. Among the various biosensors, the magnetic biosensors have attracted more attentions because of their remarkable advantages. For example, when compared to fluorescent based methods, magnetic biosensors have four advantages. First, magnetic probes are more stable over time in culture and can be used for long term labelling assays. Fluorescent tags are chemical compounds that can lose integrity as a function of time; this is not the case with magnetic nanotags. This property can prove advantageous for long term labelling assays during tissue and organ fabrication. Second, magnetic materials do not lead to background noise effects, which do occur with fluorescently labelled samples. Background fluorescence is a common phenomenon in biological samples and is due to the inherent properties of the tissue. Third,

application of controlled magnetic fields on the external surface provides a mechanism for remotely measuring and regulating the biological environment. And finally, the sensitivity of magnetic assays has been shown to be greater than fluorescent assays. The high sensitivity allows detection at significantly lower protein concentrations, compared with fluorescent based techniques (Birla, 2016). Computer aided modelling and simulation towards optimal design of biosensing systems has proven their feasible functionality and reliable performance (Nabaei, 2014). Simulation enables product comparison in a range of complex physiological environments. Therefore, prototype fabrication cost will be decreased due to optimum design of the material and instrument. However, computational modelling is not always a straightforward approach and it is accompanying with major challenges that may hamper the development of new concepts. Despite considerable advances in computing systems and methodologies in the last decade, modelling and simulation has not yet fully realized the potential and opportunities afforded by different technologies, and this has kept modelling from achieving its fullest potential in modelling complex and very large-scale systems.

Additional aspect is uncertainty. Models are necessarily approximate representations of real systems. There are always inherent uncertainties in the data used to create the model, as well as the behaviours and processes defined within the model itself. It is critical to understand and manage these uncertainties in any modelling approach. Modelling of magnetic biosensing systems are not exceptional from these difficulties. A specific challenge in this area is the need to consider

\* Corresponding author.

E-mail address: [Hadi.Heidari@Glasgow.ac.uk](mailto:Hadi.Heidari@Glasgow.ac.uk) (H. Heidari).

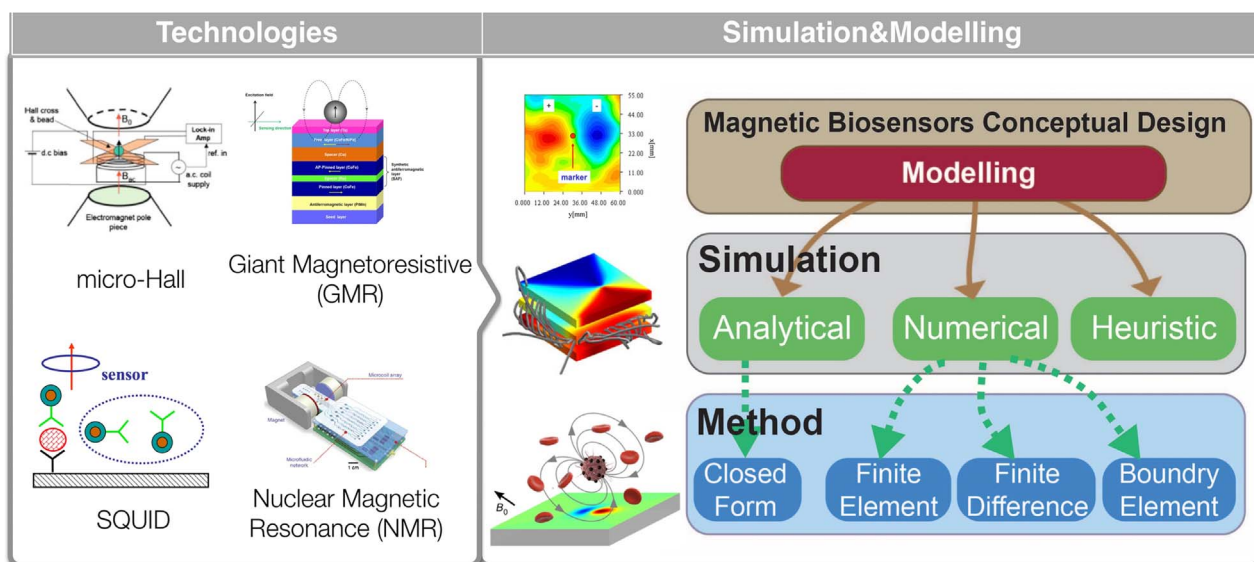


Fig. 1. Graphical overview of this review.

a wide array of relevant physical phenomena in the system. For instance, in the modelling of Hall sensor response to a localized magnetic field produced by a magnetic tip with bias voltage, a strong effect due to capacitive coupling between the tip and the sensor arises (Heidari et al., 2015). This perturbing effect appears in the measurements and it should be modelled to reach a more realistic and valuable simulation result (Heidari et al., 2013; Nabaei et al., 2013). Another main challenge is the scale of the system to be modelled and consequently the run time of the simulation work. For example, in finite element method (FEM) based modelling for a good trade-off between accuracy and simulation run time, the meshed structures of the sample should contain a sufficient number of points. Smaller meshing dimensions and higher number of points increase the accuracy of the simulation results, but would require more central processing unit (CPU) time and longer execution. One of the recent and effective techniques which have been used to overcome to this problem is *General-purpose computing on graphics processing units* (GPGPU) that uses a GPU, which typically handles computation only for computer graphics, to perform computation in applications traditionally handled by the CPU.

Different groups have worked on magnetic biosensors review, as instance, one group has focused on magnetic impedance biosensors (Wang et al., 2017). They have first introduced the magnetoimpedance effect in some soft ferromagnetic devices, and then they have reviewed the detection of magnetic ferrofluid, magnetic beads, magnetically labelled bioanalytes and biomagnetic fields of living systems. Finally, some strategies have been proposed for design of the high-performance magnetoimpedance biosensor, for quantitative and ultrasensitive detection of magnetically labelled biomolecules. Another team have reviewed three types of biosensors including magnetic relaxation switch assay-sensors, which are based on the effects magnetic particles exert on water proton relaxation rates, magnetic particle relaxation sensors, which determine the relaxation of the magnetic moment within the magnetic particle, magnetoresistive sensors, which detect the presence of magnetic particles on the surface of electronic devices (Sagadevan and Periasamy, 2014). Nano-scaled biosensors trends and their applications have been reviewed in another work (Koh and Josephson, 2009). In this study, the attention has been mainly focused on nano-structured materials, nano-particles, carbon nanotubes, and biological nanomaterial based biosensing devices.

This review presents an overview of magnetic biosensor modelling and simulation which have been developed in the past 10 years, focusing on their mathematical models and solution methodology (such as analytical and numerical). The applied model's strengths and

weaknesses are highlighted and the used competence of different modelling software, including commercial (i.e. Multiphysics modelling software) and home-made, are discussed. The objectives of this survey paper on magnetic biosensor modelling are threefold: (1) to address effective and competent magnetic biosensor modelling approaches; (2) to discuss challenges and difficulties in this area and propose possible solutions to overcome these challenges, (3) to introduce performed experimental works on magnetic biosensor which have not applied any model, and propose modelling and simulation studies that can be developed to enhance understanding and interpretation of the obtained results and optimization of the system.

## 2. Magnetic biosensors

This section reviews various representative low-magnetic field sensors and presents a brief overview of the different techniques and mechanisms as well as major results obtained so far in the development and application of these sensors.

### 2.1. Magnetoresistance device

In 1857, William Thomson (Lord Kelvin) first reported the anisotropic magnetoresistance (AMR) effect, observing that when iron was subjected to a magnetic field there was a 0.033% increase in its electrical resistance (Thomson, 1856). This very subtle effect is the result of the variation of electron mean free path as a function of the angle of the electron velocity with respect to material magnetization. The sensitivity of magnetoresistive (MR) materials is expressed as the change in resistance divided by the minimum resistance (MR ratio) (Fig. 1).

### 2.2. Giant magnetoresistance coupled multilayer

The giant magnetoresistance (GMR) effect happens in a multi-layer structure in which magnetic and non-magnetic thin films are deposited alternately. When there is no external magnetic field, the magnetization of all ferromagnetic layers is coupled to their neighbours oppositely. At this state, electron spins with both orientations are in low conductance spin channels due to the spin collision at the interfaces between ferromagnetic and non-magnetic layers. This state is called the high resistance state (Fig. 2A). When we apply an external magnetic field, all the ferromagnetic layer's magnetization is saturated in the field direction. At this state, the electron spins with the orientation in the same direction as the external magnetic field do not have spin collisions at

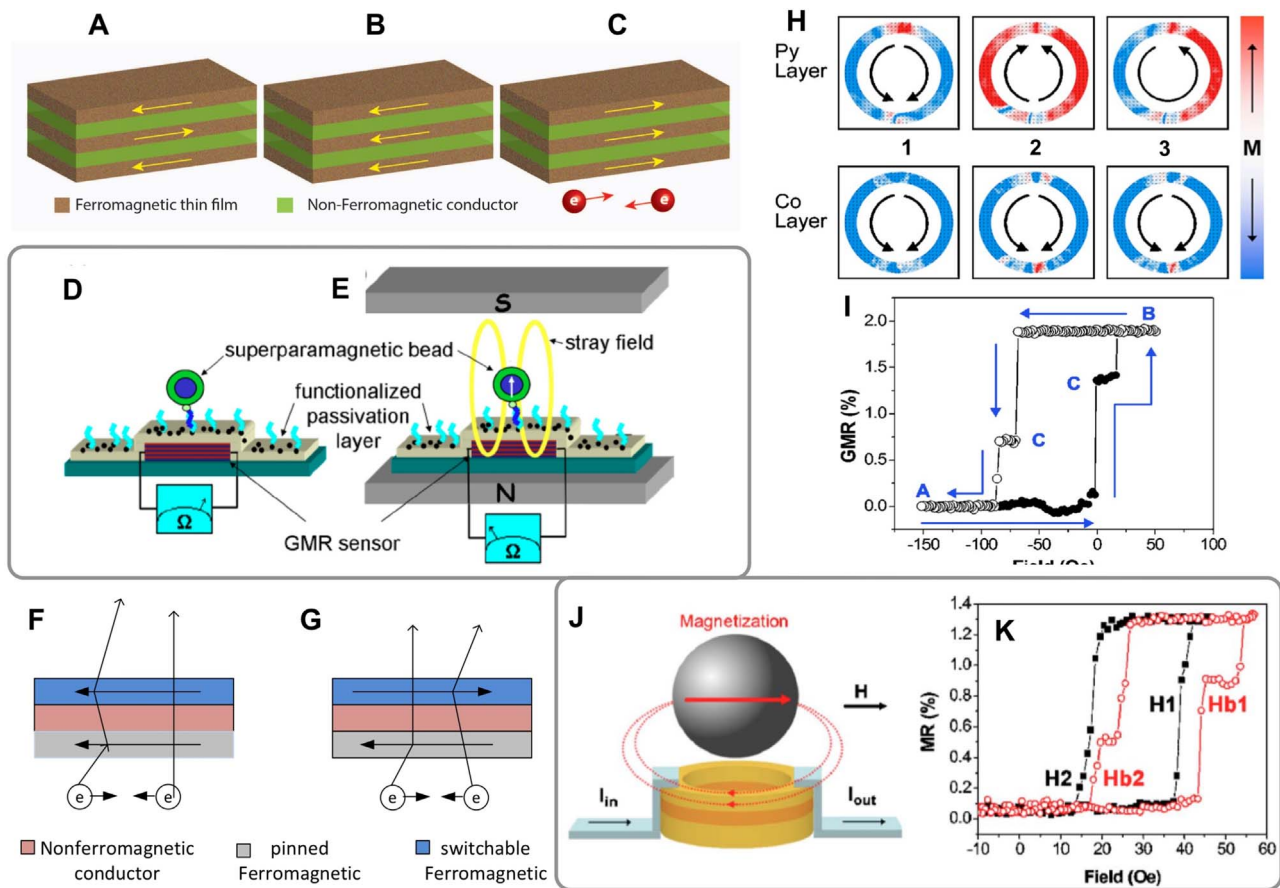


**Fig. 2.** (A) Schematic diagram of a current in plane GMR structure: magnetization of all ferromagnetic layers is coupled oppositely (high resistance state). (B) and (C) magnetization of all ferromagnetic layers are saturated in one direction by an external field (low resistance states). Schematic representation of a magnetic biosensor: (D) a superparamagnetic bead functionalized with a receptor molecule hybridize to the target molecule attached onto the sensor surface; (E) An external field align the magnetic moment of the bead and the magnetic stray field can be detected by the GMR sensor (Binasch et al., 1989). Schematic diagram of the spin-valve structure and operation of current perpendicular to the plane of GMR spin-valve at (F) parallel (low resistance) state and (G) antiparallel (high resistance) state. (H) Simulations and measured MR response of PSV ring. Micromagnetic simulations (using OOMMF) show magnetization states of a  $2 \mu\text{m}$  PSV ring with 200 nm line width as the Py layer is cycled from reverse onion (H1) to forward onion state (H2) and back, as indicated by the arrows. MR measurements on an actual microfabricated ring confirm that the reverse onion state of the Co layer remains largely undisturbed during the cycling, giving rise to minimum (H1) and maximum (H2) MR levels. The plateaus correspond to vortex states (H3) in the Py layer obtained on the ascending and descending field sweeps (Corte-León et al., 2014). Results of bead detection: (J) Schematic showing the induced dipole field from a single magnetic bead partially cancelling the externally applied field over the ring. (K) Minor hysteresis loops of the  $4 \mu\text{m}$  PSV ring taken in both presence (red open circles) and absence (black solid squares) of the bead after saturating the ring at  $-1500 \text{ Oe}$  (Corte-León et al., 2014). Reprinted with permissions. (For interpretation of the references to color in this figure legend, the reader is referred to the web version of this article).

the interfaces, thus they are in a high conductance spin channel. This state is called the low resistance state (Fig. 2B and C).

Since the GMR systems are able to sense very low magnetic fields, the potential of GMR for magnetic bead detection was realized and led to development of magnetic biosensor for life science applications. GMR effect was first described independently by Baibich et al. (1988) and Binasch et al. (1989) through the study of magnetic properties of magnetic and nonmagnetic metal thin film multilayers. Baselt et al. (1998) described a new concept in biological labelling and magnetic sensor detection based on GMR sensors.

They introduced a semiconductor-based multilayer GMR sensor chip, which came to be known as the bead array counter chip that detects local in-plane magnetic fields produced by paramagnetic microbeads immobilized directly above the sensor surface during antibody–antigen binding assays. Other investigators have also followed Baselt's initial approach with other GMR sensor devices (Reiss et al., 2005; Schotter et al., 2002, 2004). The principle detection is shown in Fig. 2D and E. Specific antigens are immobilized on the sensor surface. Superparamagnetic nanoparticles or beads, which are specifically attached to a target antibody, are used for detection. In a washing step, unbound magnetic beads are removed and beads bound to antigen molecules are measured. The superparamagnetic nature of the beads

allows to switch on their magnetic stray field by a homogeneous external magnetic field oriented perpendicular to the sensor surface (Fig. 2E). Hence, the stray field components of the magnetic markers within the sensitive sensor area can be detected by a drop in the electrical resistance of the GMR sensor. For an optimum bead detection, GMR sensors with isotropic signals and high sensitivities are needed.

Li et al. (2010) developed a GMR system that can detect interleukin-6 (IL-6), a potential cancer biomarker, in unprocessed human serum. The GMR sensor was first functionalized with capture antibodies. In the presence of IL-6, a sandwich with detection antibodies labelled magnetic nanoparticles was formed. Subsequently, dipole field generated by the particles captured on the sensor surface was detected. This method offers IL-6 detection down to  $125 \text{ fM}$  within 5 min. The assay only requires  $4 \mu\text{L}$  of serum sample for analysis, and the near  $0^\circ$  magnetization design of the GMR sensor eliminates the need for a high magnetic field. Collectively, this system has a great potential for a point-of-care device.

Some more recent works have also demonstrated that the GMR sensors are promising candidates for biomedical applications (Ennen et al., 2016; Rizzi et al., 2017; Xu et al., 2016). A CMOS front-end with integrated magnetoresistive sensors for biomolecular recognition detection applications have been reported (Costa et al., 2017). Characterization of the GMR sensor's signal and noise has shown CMOS

building blocks were designed targeting a negligible noise when compared with the GMR sensor's noise and a low power consumption. The CMOS front-end was fabricated using the magnetoresistive sensors were post-fabricated on top of the CMOS chip with high yield. Due to its low circuit noise and overall equivalent magnetic noise, the full system was able to detect 250 nm magnetic nanoparticles with a circuit imposed signal-to-noise ratio degradation of only  $-1.4$  dB. Furthermore, the low power consumption (6.5 mW) and small dimensions (7.59 mm<sup>2</sup>) of the presented solution guarantees the portability of the detection system allowing its usage at the point-of-care. A simple and sensitive method for the detection of influenza A virus based on giant magnetoresistance (GMR) biosensor has been developed in another work (Krishna et al., 2016). Authors have demonstrated GMR biosensor detected as low as  $1.5 \times 10^2$  TCID<sub>50</sub>/mL virus and the signal intensity increased with increasing concentration of virus up to  $1.0 \times 10^5$  TCID<sub>50</sub>/mL. This study has shown that the GMR biosensor assay is relevant for diagnostic application since the virus concentration in nasal samples of influenza virus infected swine was reported to be in the range of  $10^3$  to  $10^5$  TCID<sub>50</sub>/mL. Another group systematically investigated time-domain Magnetorelaxometry (MRX) by measuring the signal dependence on the applied field, magnetization time, and magnetic core size (Huang et al., 2017). MRX is a promising new biosensing technique for point-of-care diagnostics. The extracted characteristic times varied for different magnetic nano-particles (MNPs), exhibiting unique magnetic signatures. The signal contribution based on the MNP location and correlated the coverage with measured signal amplitude has been also measured. Lastly, the authors demonstrated, for the first time, a GMR-based time-domain MRX bioassay. This approach validates the feasibility of immunoassays using GMR-based MRX and provides an alternative platform for point-of-care diagnostics.

### 2.3. Spin valves

Another type of GMR effect occurs when the current is perpendicular to the film plane. This forms the basis of the so-called GMR spin-valve, which was first described by Dieny et al. (1991) It normally contains three main layers. A pinned layer, whose magnetization does not change with the external field, is normally pinned by an anti-ferromagnetic substrate, and a free layer works as a switch of the spin-valve (Fig. 2F and G). The magnetic materials could be Ni, Co and Fe. A non-magnetic conducting layer such as Cr, Cu, Ru, or Ag separates the pinned and free layers (Baibich et al., 1988; Pratt et al., 1991). When the free layer is parallel to the pinned layer the electrons, whose spins have the same orientation with the layers travel in a wide spin channel whereas the oppositely oriented electron spins have a narrow channel. When the two layers are antiparallel, electron spins in either orientation have a narrow channel in the layer with the opposite magnetization. Therefore, the resistance of a parallel state is smaller than the anti-parallel state.

This device has been used for magnetically-labelled biosensors by Graham et al. (2005, 2004) and Li et al. (2003b, 2006). Graham et al. described a  $2 \mu\text{m} \times 6 \mu\text{m}$  sensor consisting of a MR material stack with two ferromagnetic layers, typically a NiFe-based composite, which are separated by a Cu spacer to detect bulk numbers of 400 nm dextran iron oxide particles. Recent research revealed that a graphene layer can be used as the separation layer for a GMR spin-valve (Munoz-Rojas et al., 2009). Llandro et al. (2007) have presented a magnetic multiplexed assay technology which encodes the identities of target biomolecules according to the moment of magnetic beads to which they are attached. They have shown that pseudo spin valve ring can detect a single sized-matched bead in a digital manner. Simulations (using Object Oriented Micro Magnetic Framework (OOMMF) software) of the magnetization states of a Py (4 nm)/Cu (5 nm)/Co (7 nm) ring with  $2 \mu\text{m}$  outer diameter and 200 nm line width and an exemplar minor MR loop of the same structure are shown in Fig. 2H. An external magnetic field is applied to a bead placed over the ring. Since the bead

magnetization aligns with applied field, the stray field thus generated opposes and partially cancels the applied field below the bead (schematically shown in Fig. 2J). Fig. 2K shows minor MR loops taken with (red open circles) and without (black solid squares) bead over the ring. The shifts of the permally layer transition due to the dipole field generated from the bead can clearly be seen.

### 2.4. Magnetic tunnel junctions

Tunnelling magnetoresistance (TMR) is similar to GMR but has a non-magnetic insulating layer instead of a conducting one. The insulating layer is normally 1–2 nm thick, such that the electrons can tunnel through. These sensors are also known as magnetic tunnel junctions (MTJ). The materials of the insulating layer could be Al<sub>2</sub>O<sub>3</sub> (Moodera et al., 1995), Ga<sub>2</sub>O<sub>3</sub> (Li et al., 2000), MgO (Khan et al., 2008), and graphene (Cobas et al., 2012). TMR were first demonstrated independently by Moodera et al. and Miyazaki and Tezuka (Cobas et al., 2012; Khan et al., 2008; Li et al., 2000; Miyazaki and Tezuka, 1995; Moodera et al., 1995). Several groups have demonstrated the capability of TMR sensors to detect micro to nano-sized magnetic beads (Brzeska et al., 2004; Shen et al., 2005; Wang et al., 2005). MTJs are the most sensitive magnetoresistance sensors with a MR ratio of 20–50%, or, as more recently reported, over 200% when using a MgO tunnel barrier (Parkin et al., 2004b). Instead of a Cu spacer like that found in the spin-valve construction, MTJs have a thin insulating layer ( $\leq 2$  nm thick), which acts as a tunnel barrier. The thickness of the insulating layer can be varied to effectively “tune” the device sensitivity. Additionally, the sensing current is directed perpendicular to the relatively large area MTJ layers rather than in the plane of the sensor as used in GMR structures. Wang et al. (2005) are pursuing this concept to produce a  $10^6$  sensor array, with the promise of each sensor detecting a single magnetic label attached to a single DNA fragment. In a study by Albon et al. (2009) arrays of tunnel magnetoresistance sensors have been employed to detect magnetic microbeads. For single bead detection, elliptically shaped sensors of axis lengths of 400 and 100 nm are used. A linear response of the sensor signal in a magnetic field range between  $-500$  and  $+500$  Oe has been reported. An elliptical element with a length of 400 nm on the longitudinal and 100 nm on the transverse axis has been used (Fig. 3A). Magnetic markers  $1 \mu\text{m}$  Dynabead® MyOne™ are used, which are superparamagnetic and consist of about 8 nm maghemite magnetic nanoparticles embedded in a porous polymer matrix. Detection of the magnetic labels is done by applying an in-plane dc magnetic field over the linear range of the sensor. The external magnetic field is chosen parallel to the y axis (as indicated in Fig. 3B). Since the sensitivity varies between each sensor, they have introduced the relative resistance change

$$\Delta TMR = \frac{R_{bead} - R_{sensor}}{R_{sensor}} \quad (1)$$

where  $R_{bead}$  and  $R_{sensor}$  denote the resistance of the TMR sensor with and without bead, respectively. The obtained signal depends on the position of the bead with respect to the sensor (Fig. 3C). The noise signal has been evaluated by subtracting the sensor resistances between two consecutive measurements done before coating the sensor surfaces with beads. In general, for parallel orientation of the magnetization in the pinned layer and the external homogenous field, we find an increasing sensor resistance if the particle is placed along the long axis of the ellipse and a decreasing resistance value if it is located along the short axis.

### 2.5. Anisotropic magnetoresistance (AMR) based devices

The anisotropic magnetoresistance (AMR) effect leads to a local dependence of electrical conductivity on the mutual orientation of magnetization and current density vectors. The ferromagnetic sample shows high resistivity when the magnetization direction is parallel to

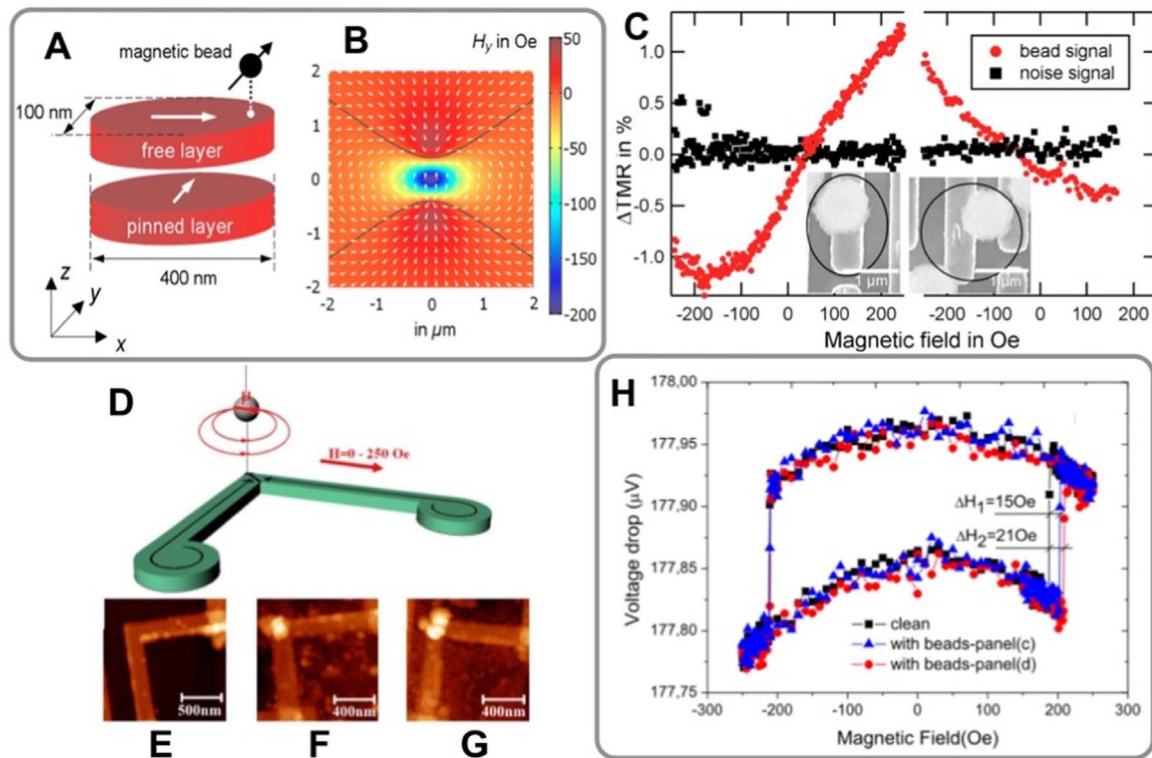


**Fig. 3.** (A) Sensor setup and initial magnetization of the ferromagnetic electrodes (Donolato et al., 2010). (B) The in-plane magnetic field of a bead with magnetic moment of 67.2 kA/m aligned parallel to the y axis. The black lines indicate the component value  $H_y = 0$ . (C) Examples of the detection of single superparamagnetic beads with respect to its orientation toward the sensor. Insets show the experimental situation (Donolato et al., 2010). (D) 3D schematic of the device interacting with a magnetized particle (Enserink, 2001). (E) AFM image of a clean device. (F) and (G) AFM images after the first and second dispensation of a drop of the same volume (2  $\mu$ L) and concentration of beads ( $5 \times 10^{10}$  particles  $\text{mL}^{-1}$ ). (H) Voltage drop across the corner as a function of the magnetic field for the clean ring (squares), with the cluster of beads of panels (c) (triangles) and (d) (circles). The field is applied starting from 0 Oe and cycled back and forth up to  $\pm 280$  Oe (Enserink, 2001). Reprinted with permissions.

the current, and low resistivity when they are perpendicular (Beguin et al., 2014; Corte-León et al., 2014; Manzin et al., 2014). Before GMR, there was an active pursuit of devices utilizing AMR (McGuire and Potter, 1975). Miller et al. (2002) introduced the use of AMR technology in the form of a ring sensor. In the ring approach, a single-layer, current-in-plane  $\text{Ni}_{80}\text{Fe}_{20}$  ring sensing element is fabricated whereby the AMR material is modulated by the radial fringing field from a single magnetic bead. The ring sensor has outer and inner diameters of 5  $\mu\text{m}$  and 3.2  $\mu\text{m}$ , respectively. When the bead is centred over the ring, the radial fringing field rotates the magnetization from circumferential towards a radial outward direction. This rotation causes a magnetoresistance to decrease and a measurable voltage signal in the Wheatstone bridge. Recently, AMR nanostructures with different shapes such as L-shape (Donolato et al., 2009), square ring (Vavassori et al., 2008), and zigzag (Donolato et al., 2010; Ruan et al., 2010; Vieira et al., 2012, 2009) have been employed for detection of magnetic beads. Donolato et al. (2009) have presented a device concept based on controlled micromagnetic configurations in a corner-shaped permalloy nanostructure terminated with two circular disks (Fig. 3D). The device consists of a patterned L-shaped permalloy strip, 25 nm thick and 180 nm wide, with two end disks (diameter 500 nm) that have their centre at 2  $\mu\text{m}$  from the corner. They have performed AMR measurements on the studied device and it can be seen from Fig. 3H the beads grouped on the corner by the domain wall (DW) can influence the position of the first transition (for positive magnetic field) corresponding to the removal of the domain wall from the corner where the beads are located. Magnetic bead detection using DW-based magnetic nanostructures (e.g. a L-shaped nanowire) and based on AMR properties of the nanostructure has two main steps; first step is pinning of the DW in the nanostructure (corner), the second step is characterization of the AMR properties of the nanostructure in the presence and absence of the magnetic bead

grouped by the DW on the corner of the nanostructure.

## 2.6. Hall magnetometry

Hall sensors are versatile devices exhibiting a high magnetic moment sensitivity over a wide field range and an elevated signal-to-noise ratio in both low and room temperature conditions (Heidari et al., 2014, 2016). Moreover, they generally provide a linear response, being not affected by magnetic saturation. These sensors have been studied and investigated both experimentally and numerically for different applications, such as Hall magnetometry on nanostructures, detection of magnetic beads as label in medical application.

## 2.7. Hall devices for detection of magnetic beads

As one of the most important applications, Hall sensors have been adopted for the detection (Besse et al., 2002; Di Michele et al., 2011; Haun et al., 2010; Kazakova et al., 2007; Landry et al., 2004; Llandro et al., 2010; Manandhar et al., 2009; Mihajlovic et al., 2007, 2005; Sandhu et al., 2007) and even counting (Lee et al., 2009) of individual magnetic nanobeads used as labels for medical imaging, drug delivery and manipulation of biological species (Gijs, 2004; Pankhurst et al., 2003). Furthermore, they can be used to map the trajectory of moving beads, as demonstrated by Aledealat et al. (2010) for the dynamic detection of superparamagnetic beads in a microfluidic channel integrated with an InAs quantum well micro-Hall sensor. As one of the pioneering groups, Besse et al. have used a cross-shaped silicon Hall sensor fabricated in CMOS technology with active area  $2.4 \times 2.4 \mu\text{m}^2$  for the detection of a single magnetic bead (Dynabead M-280) (Besse et al., 2002). Mihajlović et al. (2005) have performed a room-temperature detection of a single commercial superparamagnetic bead suitable for

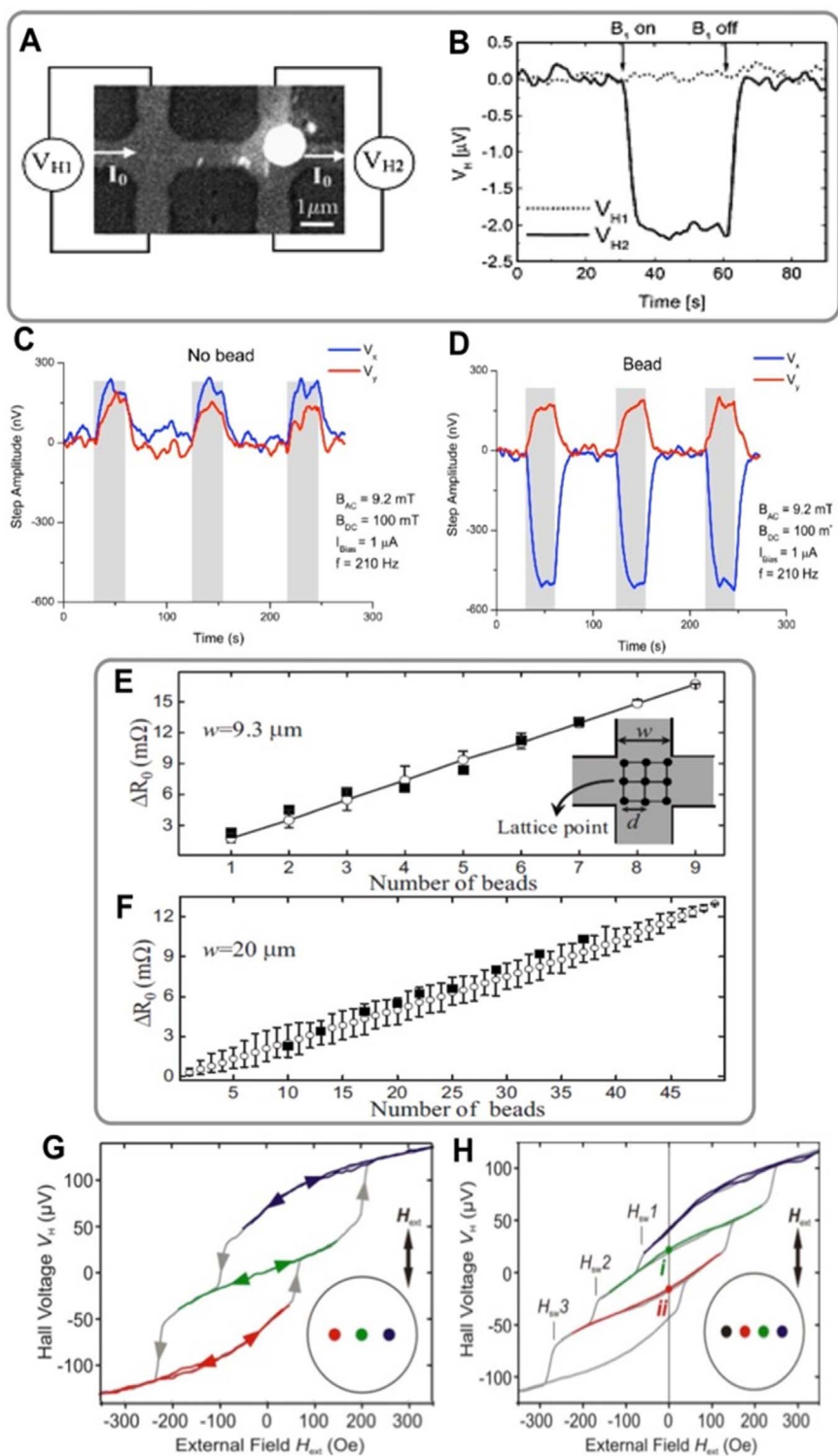


**Fig. 4.** (A) SEM image of two adjacent Hall crosses adapted to show the actual detection measurement configuration; (B) ac Hall voltage as a function of time for the two crosses shown in part (A) of the figure. The drop in the signal from one cross upon applying the static field  $B_1$  is due to the presence of the bead (Graham et al., 2004). In-phase ( $V_x$ ) and out-of-phase ( $V_y$ ) components of the ac Hall voltage in response to  $B_{DC}$  steps ( $B_{DC} = 100$  mT) with a duration of 30 s as measured on (C) an empty device and (D) a device with a Dynal bead. Note that the  $V_y$  component always shows an increase of the voltage independent of the presence of the bead. The effect is associated with dominating inductive and parasitic ferromagnetic signals. The gray rectangles represent the state when  $B_{DC}$  is on (Issadore et al. (2013)). Experimental (full squares) and calculated (open circles) Hall resistance at  $H = 0$  as a function of the number of beads. The solid lines are guides for the eyes. (E) and (F) are for the Hall sensors that are 9.3  $\mu\text{m}$  and 20  $\mu\text{m}$  in width, respectively. The inset of (E) illustrates an example of lattice points in the sensor area for calculation, where  $w$  is the width of the Hall sensor and  $d$  is 2.8  $\mu\text{m}$ , i.e., the diameter of a bead. The calculated values are an average, and the upper and lower error bars indicate the maximum and minimum values, respectively (Kazakova et al., 2007). Hall voltage loops of Permalloy disks (diameter: 800 nm, thickness: 30 nm, temperature: 1.4 K) containing three and four artificial pinning centres. The field is applied in the plane of the disks as indicated by arrows. (G) The three branches of the minor loop reflect pinning of the vortex core at different pinning sites. The blue hysteresis branch corresponds to pinning at the blue pinning site, etc. Double arrows represent reversible sections of the stray field curves, while single arrows show the direction of irreversible jumps. The antidots were separated by 200 nm. (H) Four stable magnetic states can be found in a disk with four antidots separated by a distance of 150 nm. Switching from plateau (i) to (ii) is accomplished by applying an external magnetic field between  $H_{sw2}$  and  $H_{sw3}$  (Li et al., 2000). Reprinted with permissions. (For interpretation of the references to color in this figure legend, the reader is referred to the web version of this article).

biological applications, using an InAs quantum-well micro-Hall sensor. Their studies have demonstrated the use of phase-sensitive detection on a single Hall cross as well as in a Hall gradiometry setup. Sensor geometry and test result of ac phase sensitive detection are shown in Fig. 4A and B, respectively. A clear drop in the Hall voltage is observed for the cross with the bead and it is completely absent for the empty cross. The magnitude of the voltage decrease is 2.0  $\mu\text{V}$ , which corresponds to a change in the sensed stray field of 80  $\mu\text{T}$  (Fig. 5).

Kazakova et al. have also presented detection and susceptibility measurement experiments on a single superparamagnetic bead

applying an ac-dc measurement technique (Di Michele et al., 2011, 2010; Kazakova et al., 2010). The detection and magnetic characterization of the bead were performed using ultra-sensitive InSb Hall devices. Single bead detection was demonstrated using a step-wise change of the dc magnetic field; measurements were performed using only the in-phase component of the total ac Hall voltage. Very clear evidence of the bead presence was simultaneously demonstrated with explicit separation of parasitic inductive signals (Fig. 4C and D).

The Hall sensors have also been employed for the counting of magnetic beads by Lee et al. (2009). For this purpose, Hall resistances

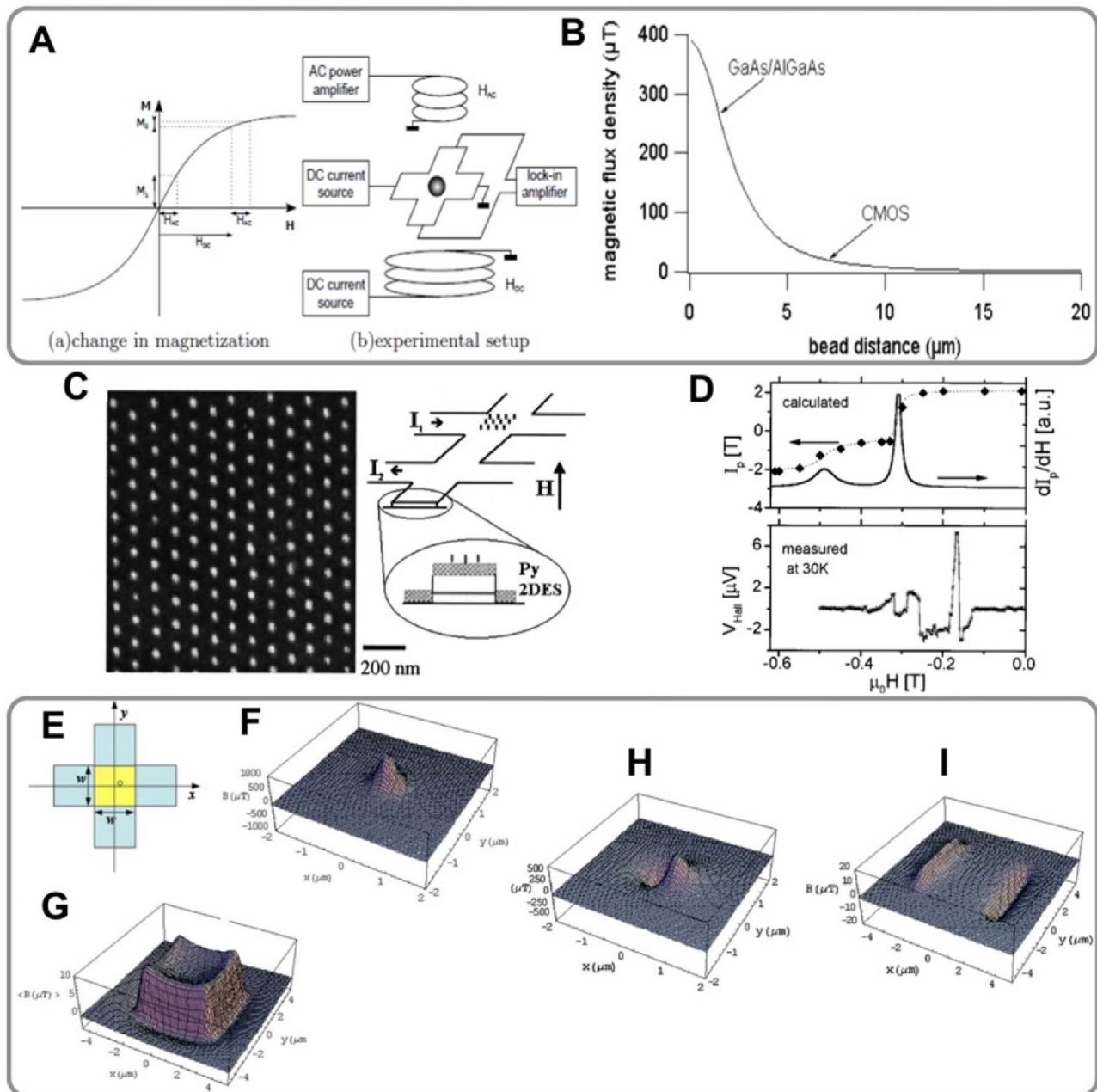


**Fig. 5.** (A) Single bead detection experiment (Mihajlovic et al., 2005). (B) Influence of bead distance from sensor (Mihajlovic et al., 2005). (C) SEM image of an iron particle array grown onto Permalloy (where the particles with diameters of about 13 nm are arranged on a hexagonal lattice) and setup of the magnetic measurements (Miller et al., 2002). (D) Comparison of calculated (top) and measured (bottom) Magnetization reversal for a particle-Permalloy heterostructure. The calculated total magnetization of the particles,  $I_p$  and its derivative  $dI_p/dH$  show clearly a reversal in two steps. The measured Hall voltage can favourably be compared to  $dI_p/dH$ . Again, a sharp and a broader step due to the particles' influence can be recognized (Miller et al., 2002). (E) Coordinate system used in the calculations, and simulation results (Miyazaki and Tezuka, 1995): (F) Perpendicular component of the magnetic field from a magnetic bead in a direction perpendicular to the sensor plane, (G) magnetic field detected by the Hall sensor as a function of bead position, (H) perpendicular component of magnetic field from a magnetic bead in a direction horizontal to the sensor plane, and (I) magnetic field detected by the Hall sensor as a function of bead position (Miyazaki and Tezuka, 1995). Reprinted with permissions.

measured at room temperature are found to be proportional to the number of the magnetic beads (Fig. 4E and F), and are in good agreement with the numerically simulated results presented in this study. Proposed sensors are designed to measure the number of beads between zero and full-scale signals for a given number range of interest.

A microfluidic chip-based micro-Hall ( $\mu$ Hall) platform for sensitive detection of bacteria was recently reported (Issadore et al., 2013). In this approach, target bacteria (*Staphylococcus aureus*) were magnetically labelled using molecular ligands, rendering them superparamagnetic. The local magnetic fields produced by individual bacteria were then measured by the  $\mu$ Hall sensors. This system enables bacteria detection

within 1 h over a wide dynamic range ( $10^1$ – $10^6$  counts) and the authors demonstrated the ability to distinguish Gram-positive from Gram-negative bacteria. By changing the molecular ligands, this assay could be adapted to differentiate a variety of other bacterial species.

### 2.8. Hall magnetometry on magnetic nanostructures

The magnetic behaviour of sub-micrometre ferromagnetic elements has become increasingly important because of their application in magnetoelectronic devices. These devices typically contain a patterned soft magnetic layer which is switched between two magnetization states

(Manzin and Nabaei, 2014). Micro and nanostructured permalloy media are a possible candidate for such devices (Gallagher et al., 1997; Gomez et al., 1999; Kirk et al., 1997). In particular, with circular nanomagnets made of permalloy or cobalt, it might be possible to realize the needed micromagnetic characteristics (Cowburn et al., 1999; Guslienko et al., 2002; Prejbeanu et al., 2002; Pulwey et al., 2001; Raabe et al., 2000; Schneider et al., 2002, 2000). Hall-magnetometry, imposing a negligible perturbation on the nanomagnet during the magnetization reversal process, has been introduced as a powerful tool for the detection of nanostructure stray field. An important advantage of this method is that it can be employed over a wide range of temperatures, i.e. from cryogenic temperatures up to ambient temperature. This technique has been used by different groups to measure stray field hysteresis loops of different nanostructures (Hengstmann et al., 2001; Rahm et al., 2003a, 2003b; Schneider et al., 2003; Schuh et al., 2001). Rahm et al. (2003b) have used Hall sensors fabricated from GaAs/AlGaAs heterojunction material to measure stray field hysteresis loops of individual disks. Hall magnetometry on individual ferromagnetic disks has also been performed to study vortex pinning at single point defects (Rahm et al., 2004a). As a main conclusion, the authors showed, by using Hall magnetometry, that point defects inside ferromagnetic disks can significantly alter the corresponding hysteresis trace. By means of Hall magnetometry, it has been also put in evidence that inserting  $n$  antidots (holes) into a disk the magnetization reversal takes place via  $(n-1)$  jumps of the vortex core between neighbouring antidots (Rahm et al., 2004b). The results of this study are shown in Fig. 4G and H. It can be seen from measurements that each defect represents an artificial pinning site for the magnetic vortex core. Besides experimental Hall magnetometry on nanostructures, analytical studies also show that the introduction of a hole into a ferromagnetic nanodisk may deeply modify the structure and dynamics of a vortex like state (Moura-Melo et al., 2008)

### 2.9. Hall sensor response to local electric and magnetic fields

Scanning gate microscopy (SGM) is a technique that can be used to explore magnetic sensitivity of Hall effect sensors. In this technique, the measured quantity is the transverse Hall voltage of the device while the magnetic tip is scanned over the sensor surface. The magnetic tip, conventionally used for magnetic force microscopy, is here used as a source of stray magnetic field to be detected by Hall effect sensors (Nabaei et al., 2013). The magnetic tip can be also electrically charged and thus capacitively coupled to the sensor plane, due to the application of a voltage bias or contamination phenomena, producing perturbing electric fields. This phenomenon has been investigated through numerical modelling and experimental analysis in (Nabaei et al., 2013). Folks et al. have measured the room temperature response of nanoscale

semiconductor Hall crosses to local applied magnetic fields under various local electric gate conditions using scanning gate microscopy. In this study, near-surface quantum wells of AlSb/InAs/AlSb, located just 5 nm from the heterostructure surface, allow very high sensitivity to localized electric and magnetic fields applied near the device surfaces. The Hall crosses have critical dimensions of 400 and 100 nm. With certain small gate voltages ( $V_g$ ) the devices of both sizes are strongly responsive to the local magnetic field at the centre of the cross. The authors have found that, at high  $V_g$ , the response to local magnetic fields is greatly distorted by strong electric fields applied near the cross corners (Folks et al., 2009). Baumgartner et al. (2006) have presented scanning gate measurements on a Hall cross in the regime of the classical Hall effect. The real-space patterns of induced resistance changes are manifestations of the symmetry properties of such a Hall system. The detailed behaviour in the diffusive regime has been shown to be compatible with models based on a local conductivity tensor. Hall cross geometry sensor also have been used as a local electric field probe, which is capable of detecting an electric charge as small as the charge of one electron, operating under ambient conditions and having a spatial resolution down to 100 nm (Barbolina et al., 2006). The submicron-sized probes were made from a high-density high-mobility two-dimensional electron gas, which is sensitive to the presence of electric charges near its surface. The authors demonstrate the possibility of using such microprobes for life-science applications by measuring an electric response of individual yeast cells to abrupt changes in their environment.

### 2.10. Superconducting quantum interference device (SQUID)

One of the most sensitive low field sensors is the superconducting quantum interference device (SQUID) (Tamanaha et al., 2008) developed around 1962 with the help of Brian J. Josephson's work (Lenz, 1990). Kotitz et al. (1997) first introduced the concept of SQUID to detect antibodies labelled magnetic nanoparticles as a way to avoid using radioisotopes or unstable enzymes or fluorescent dyes that are standard in immunoassays. Externally applied magnetic field magnetizes the superparamagnetic nanoparticles such that they line up along the magnetic field lines. When the magnetic field is removed, the particles remain aligned for a brief period before randomizing again. This short, but decaying, period of self-magnetization is described as a magnetic remanence. A SQUID measures the decay of remnant magnetization of superparamagnetic nanoparticles bound to targets. In another SQUID measurement technique, Enpuku et al. (2005) and Tsukamoto et al. (2005) developed a 25 nm-diameter (nominal)  $\text{Fe}_3\text{O}_4$  magnetic marker with a high magnetic field and designed an optimized pickup coil to detect the magnetic flux signal from a moving sample.

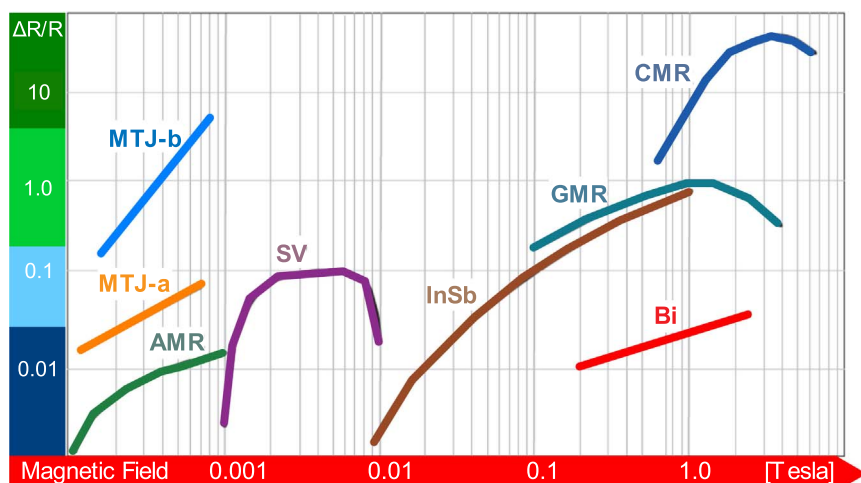


Fig. 6. Various magnetoresistance effects. Reproduced from Tumanski (2001, 2016).



### 3. Discussion

Among the various magnetoresistive effects (Fig. 6), AMR effect, GMR, spin valve effect and magnetic tunnel junction MTJ are commonly being used (Tumanski, 2001). Despite the fact that the AMR sensors are treated as slightly old-fashioned sensors but they have interesting advantages. They are very cheap and still available. The AMR sensors have better sensitivity than GMR sensors. In these sensors preparation of pairs of sensors to remove the influence of the temperature is easy. In contrary, the main disadvantages of AMR sensors are relative small change of resistance, not exceeding 2% and possibility of demagnetization by high magnetic field. The GMR sensors in two thin ferromagnetic films, transition from initial antiparallel to parallel state is accompanying by a very large (even more than 100%) change of resistance. The main disadvantage of classical GMR effect was pure sensitivity. Antiparallel state was obtained by strong coupling of two layers separated by very thin separator. The MTJ sensors with spacer made by oxidized aluminum have quite large magnetoresistance about 40% for relative small magnetic field (Fig. 6). But this type of MTJ had some problems with noises and small polarization voltage. Another type of MTJ with barrier of crystalline textured MgO has magnetoresistance as large as 180–220% (Parkin et al., 2004a; Yuasa et al., 2004).

Hall effect devices with simple design and technology of manufacturing are most widely used magnetic sensors. They are very cheap but the sensors for magnetic field measurement with high linearity and small temperature errors are expensive. Other remarkable advantages of these sensors are the lack of ferromagnetic elements and the possibility of measuring of the various parameters such as current, angle, radial and axial position. The offset voltage of a Hall device is a quasi-static output voltage that exists in the absence of a magnetic field. It severely limits the applicability of Hall sensors when non-periodic or low frequency magnetic signals have to be detected. Relative low sensitivity and high consumption are the other drawbacks of these devices. It is important to note that using high mobility material for Hall sensors lead to high sensitivity and low offset. It should be also noted that miniaturization of the hall sensors deteriorates their performance and this deterioration can be compensated by the associated electronic circuit, but this implies a rising of the development costs. The highest sensitivity exhibits SQUID sensors with noise about  $5 \text{ fT}/\sqrt{\text{Hz}}$  enable to detect fTmagnetic field. Therefore they are suitable for magnetic field resulting from brain activity. The NDT techniques also profit this high sensitivity to detect and even to forecast defects (Krause and Kreuzbruck, 2002). One of the drawbacks of the SQUID devices is that the application of this type of magnetic sensors is restricted to low temperature condition.

Magnetic sensors working range and a category of magnetic sensors applications are presented in Fig. 7 and Table 1 (Lenz and Edelstein, 2006). As can be seen, magnetic sensors have a broad range of applications. For example, ultra-sensitive magnetic sensors are able to detect tiny magnetic fields produced outside the brain by neuronal currents,

which can be used for diagnostic applications. High reliability non-contact switching with magnetic sensors leads to enhanced safety standards in aircraft, and magnetic sensors are also used in automobiles to detect positions in the engine crank shaft and wheel braking. Computers have nearly unlimited memory through the application of magnetic sensors in magnetic storage hard drives and tape drives (Nazari Nejad, 2015).

### 4. Modelling and simulation of magnetic biosensors

#### 4.1. Finite element modelling and methodology

There are a great many numerical techniques used in engineering applications for which digital computers are very useful. The numerical techniques generally employ a method which discretizes the continuum of the structural system into a finite collection of points (or nodes)/elements called finite elements. The most popular technique used currently is the finite element method (FEM). There are other methods like the finite difference method (FDM) and the boundary element method (BEM).

#### 4.2. Finite element method

In the finite element method (FEM) of analysis a complex region defining a continuum is discretized into simple geometric shapes called finite elements. The material properties and the governing relationships are considered over these elements and expressed in terms of unknown values at elements corners. An assembly process duly considering the loading and constraints results in a set of equations. Solution of these equations gives the approximate behaviour of the continuum. The basic steps in the FEM are: (1) Discretization of the domain; (2) Identification of variables; (3) Choice of approximating functions; (4) Formation of the element stiffness matrix; (5) Formulation of the overall stiffness matrix; (6) incorporation of boundary conditions; (7) Formulation of element load matrix; (8) Formation of the overall load matrix; and (9) Solution of simultaneous conditions. The advantages of FEM are: (a) fast, reliable and accurate; (b) it can analyse any structure with complex loading and boundary conditions; (c) it can analyse structures with different material properties; (d) this method is easily amenable to computer programming; and (e) it can analyse structures having variable thickness. Main disadvantages of this method are: (a) the cost involved in the solution of the problem; (b) it is difficult to model all problems accurately and the results obtained are approximate; (c) the result depends upon the number of elements used in the analysis; and (d) data preparation is tedious and time consuming.

#### 4.3. Finite difference method

In the finite difference approximation of differential equations, the derivatives in the equations are replaced by difference quotients of the

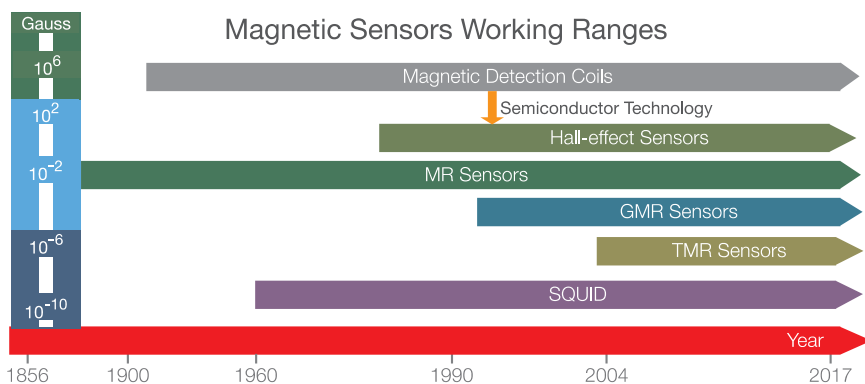


Fig. 7. Comparison between magnetic sensors working range.

**Table 1**  
Category of magnetic sensor applications.

Magnetic field	1 nT	1 $\mu$ T	10 mT
Category	<i>High Sensitivity</i>	<i>Medium Sensitivity</i>	<i>Low Sensitivity</i>
Definition	Measuring field gradients or differences due to induced (in Earth's field) or permanent dipole moments	Measuring perturbations in the magnitudes and/or direction of earth's fields due to induced or permanent dipoles	Measuring fields stronger than Earth's magnetic field
Major Applications	Brain function mapping magnetic anomaly detection	Magnetic compass Munitions fusing Mineral prospecting	Noncontact switching Current measurement Magnetic memory readout
Most Common Sensor	SQUID Optically pumped	Coil magnetometer Fluxgate Magnetoresistive	Coil magnetometer Hall-effect sensor Magnetoresistive

values of the dependent variables at discrete mesh points of the domain. After the equations are replaced by difference quotients of the values of the dependent variables at discrete mesh points of the domain. After imposing the appropriate boundary conditions on the structure, the discrete equations are solved obtaining the values of the variables at mesh points. The technique has many disadvantages, including inaccuracies of the derivatives of the approximated solution, difficulties in imposing boundary conditions along curved boundaries, difficulties in accurately representing complex geometric domains, and the inability to utilize non-uniform and non-rectangular meshes.

#### 4.4. The boundary element method

The boundary element method developed more recently than FEM, transforms the governing differential equations and boundary conditions into integral equations, which are converted to contain surface integrals. Because only surface integrals remain, surface elements are used to perform the required integrations. This is the main advantage of BEM over FEM, which require three-dimensional elements throughout the volumetric domain. Boundary elements for a general three-dimensional solid are quadrilateral or triangular surface elements covering the surface area of the component. For two-dimensional and axisymmetric problems, only line elements tracing the outline of the component are necessary. Although BEM offers some modelling advantages over FEM, the latter can analyse more types of engineering applications and is much more firmly entrenched in today's computer-aided-design (CAD) environment. Development of engineering applications of BEM is proceeding however, and more will be seen of the method in the future.

#### 4.5. Hall effect devices

The Hall effect sensors can be used for the detection of magnetic beads (Colle, 2008). Using the superparamagnetic behaviour of magnetic beads, a simulation model for the bead detection has been developed and have applied ac-dc technique to perform experimental studies (Fig. 5A). They have concluded that the Hall voltage obtained from CMOS sensors can be improved by decreasing the passivation (Fig. 5B) and for heterostructure sensors a different material stack might be able to decrease the detection limit. In this paper authors have pointed that a finite element method (FEM) simulation has been applied to validate the proposed mathematical model of dipole approximation between the bead and Hall sensor.

Magnetization processes in arrays of ferromagnetic iron particles with diameter about 13 nm, have been investigated by Christoph et al. (2001) (Fig. 5C). A modified boundary-element method was developed to calculate the magnetization pattern of the particle-Permalloy heterostructures with a proper discretization of the system. This method simplifies the evaluation of the magnetostatic energy, a difficult problem encountered in using FEM. The calculated magnetic behaviour of the Permalloy film, the particles, as well as the coupled heterostructure for applied fields has been compared to the experimental magnetization

curves (Fig. 5D). Magnetization reversal for an array of  $5 \times 5$  particles interacting via magnetic Permalloy layer is calculated (Fig. 5D, top panel). Only the particle magnetization  $I_p$  is shown. Magnetization reversal of the particles started at fields as small as  $\mu_0 H_0 = -0.25$  T and completed at  $\mu_0 H_0 = -0.6$  T. As a consequence of the Hall gradiometry, the measured voltages resulted from differences in the magnetization of heterostructures compared to Permalloy without carrying an array. Strong influences due to the particle magnetization reversal were observed from  $-0.15$  T (with a sharp onset) up to fields of  $-0.32$  T at 30 K (Fig. 5D, bottom). It is a remarkable result of the numerical simulation that the net remagnetization curve of the Permalloy layer was only weakly influenced by the iron particles (also seen experimentally by the small total Hall voltage, Fig. 5D, bottom) but the domain patterns differed strongly. This can be understood as being due to the local character of the particle stray fields.

Kumagai et al. (2008) have proposed a numerical and experimental analysis on the variation of the magnetic sensitivity of the active surface region of AlGaAs/InGaAs two-dimensional electron gas Hall effect biosensors with location and number of superparamagnetic beads. Detection procedure of superparamagnetic beads with diameters in the range of 200 nm to 2.8  $\mu$ m using Hall sensors and lock-in measurements has been already reported in a previous work (Sandhu et al., 2004). They have simulated how the magnetization both in the vertical and horizontal components of the beads' magnetization influences the output of the Hall sensor. Fig. 5E shows the coordinate system used in their numerical analysis of the Hall sensors. Fig. 5F shows the perpendicular component of the magnetic field from a magnetic particle saturated perpendicular to the sensor plane, deduced using analytical equations (Sandhu et al., 2004). Fig. 5G is magnetic field detected by the 5  $\mu$ m Hall sensor as a function of position of 1  $\mu$ m magnetic bead shows the perpendicular component of the magnetic field from a magnetic bead magnetized in the horizontal direction to the sensor plane. Fig. 5I is magnetic field detected by the Hall sensor as a function of position of magnetic bead, while the bead is magnetized in the horizontal direction. Performed analysis showed that edges and corners of the Hall sensors were most sensitive and exhibited a linear response.

Sandhu et al. (Kim et al., 2015). have fabricated an on-chip magnetometer by integrating a planar Hall magnetoresistive (PHR) sensor with microfluidic channels. The PHR signals were monitored during the oscillation of 35  $\mu$ L droplets of magnetic nanoparticles. A FEM simulation using Maxwell software (Ver. 12.2, Ansoft, USA) has been carried out to determine the critical length of a droplet for an undistorted dipole field. The maximum length of the mesh was set to be 1.5  $\mu$ m. The permanent magnets were introduced for the generation of a magnetic field in the magnetostatic model of the Maxwell 3D software. The measured M-H curve for 3  $\mu$ L sample was used as an input parameter in Maxwell software. Field distribution was generated by entering the M-H curve data in the Maxwell software. The simulated results are shown in Fig. 8A, contour flux lines of a droplet under an applied field of +100 Oe in the z-direction. The distribution of simulated  $B_x$  is plotted in Fig. 8B, because the sensor is sensitive to the in-plane

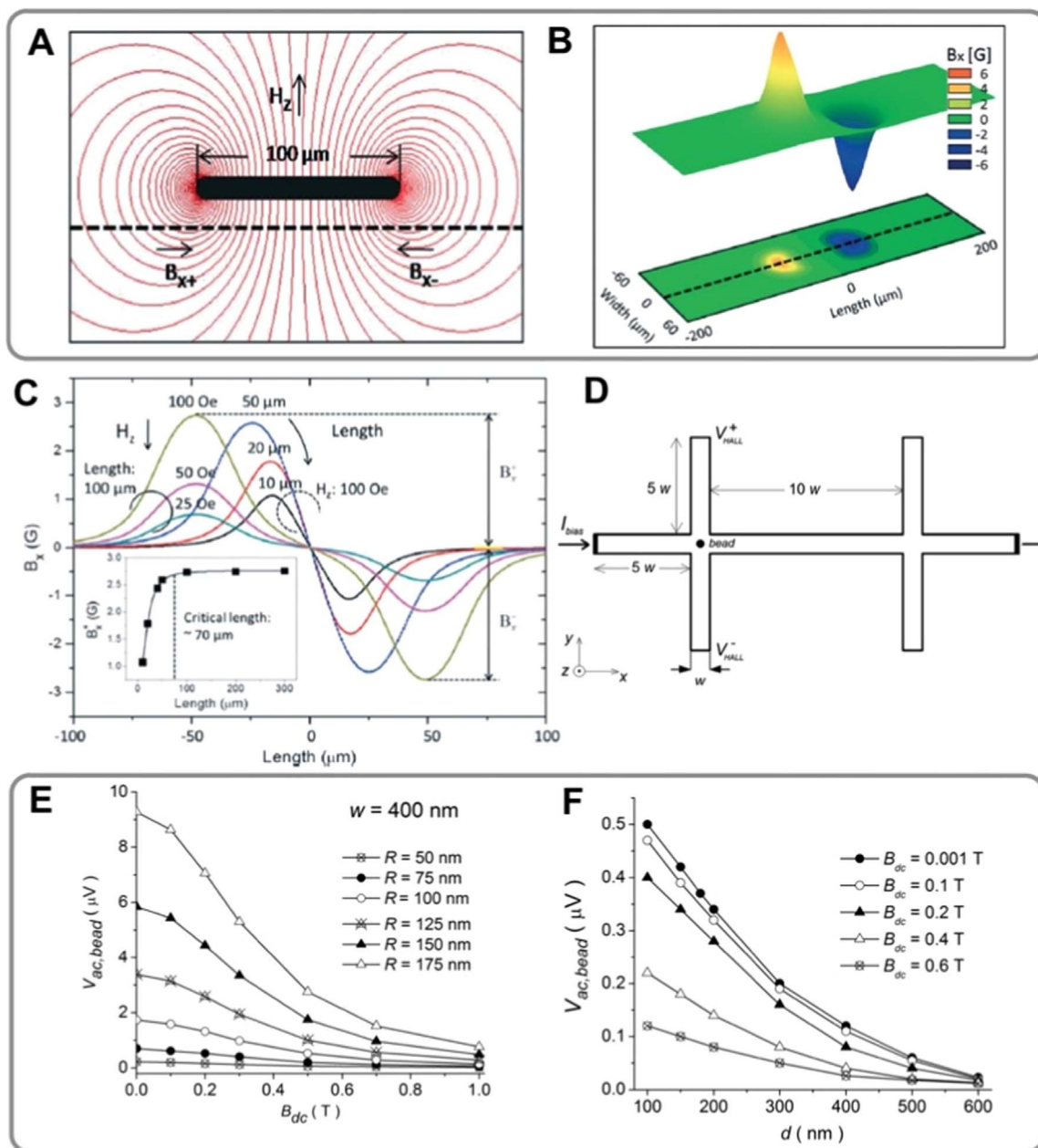


**Fig. 8.** (A) The contour flux lines of a droplet under an applied +100 Oe z-field (Moura-Melo et al., 2008). (B) The contour of  $B_x$  field (Moura-Melo et al., 2008). (C) The simulated profiles of various lengths of droplets, and the inset shows the critical length of droplet (above  $70 \mu\text{m}$ ) in which the droplet signals are apparent (Moura-Melo et al., 2008). (D) Scheme of the double-cross Hall sensor. The nanobead is located in correspondence of the left cross centre. The Hall voltage is computed as the difference between the average electric potential values at the voltage lead ends (Munoz-Rojas et al., 2009). (E) Amplitude of the ac Hall voltage due to a nanobead with variable radius  $R$  as a function of dc magnetic field. The vertical distance between the Hall plate and the bead centre is  $200 \text{ nm}$ . The probe width  $w$  is set at  $400 \text{ nm}$  (Nabaei et al., 2013). (F) Amplitude of the ac Hall voltage due to a  $75\text{-nm}$ -radius bead as a function of the dc field and the distance  $d$  from the bead centre to the Hall plate. The probe width  $w$  is equal to  $600 \text{ nm}$  (Nabaei et al., 2013). Reprinted with permissions.

component  $B_x$ . The profiles of  $B_x$  along the centre line for a range of lengths of droplets are shown in Fig. 8C. An increase in the length of a droplet leads to an increase in the peak of dipole field strength up to a droplet length of  $70 \mu\text{m}$ , after which it is invariant (Fig. 8C and the inset). The decrease of the peak for droplet lengths smaller than  $70 \mu\text{m}$  is caused by the overlapping of positive and negative fields at the edges of the droplets. These results showed that the critical length of a droplet for undistorted field information was  $70 \mu\text{m}$  for  $25 \mu\text{m}$  height and  $20 \mu\text{m}$  width. Simulation gave an idea about the size and distance of the droplet to be detected, and helped to design and prepare an optimum and effective experimental setup in this study.

Manzin et al. (2012) have introduced Hall sensors model for detection of magnetic nanobeads using FEM. The *ac-dc measurement*

*technique* has been selected for this purpose. A two-dimensional model has been developed under the assumptions of diffusive transport regime. The magnetic described as a dipole and is assumed to be uniformly magnetized along the external applied field.

In this work, a Hall sensor with variable probe width ranging from  $400 \text{ nm}$  to  $800 \text{ nm}$  has been modelled. Fig. 8E shows the amplitude of the Hall signal due to the bead versus applied DC magnetic field. As it can be seen, an increase of the dc field leads to a detriment in the magnetic moment resolution. As the other parametric analysis, a  $75\text{-nm}$ -radius bead is placed at different heights above the Hall sensor. Fig. 8F shows that for high values of magnetic dc field, the influence of height on hall signal reduces. The model used for simulations in this work has been developed at INRIM (Istituto Nazionale di Ricerca

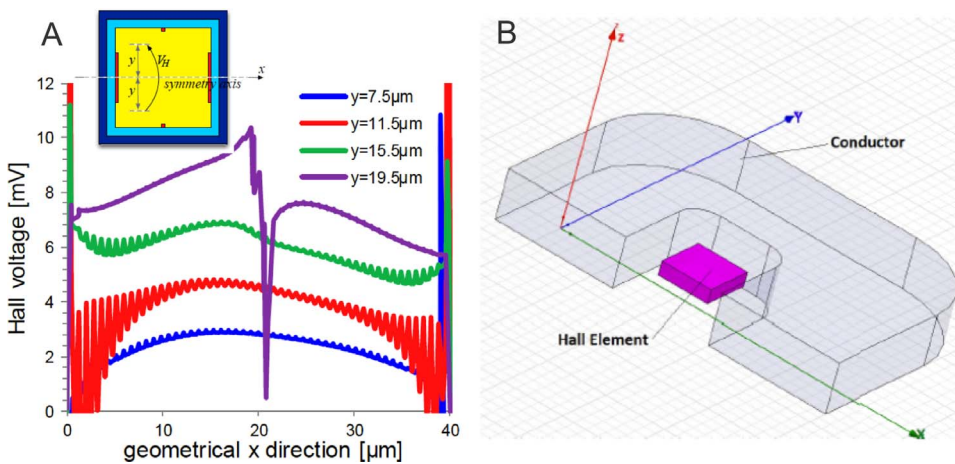


Fig. 9. (A) Simulation Hall voltage along x direction for a  $40 \mu\text{m} \times 40 \mu\text{m}$  sensor and (B) Simulation Model (Crescentini et al., 2017).

Metrologica, Turin, Italy) based on the FEM. This home-made model is advantageous to the models developed in commercial Multiphysics software, because of its high flexibilities in introducing various states and working conditions as well as high capability to be modified and extended for simulation of different problems and applications.

The effects of design parameters on the performance of a general CMOS Hall sensors, with insight on current-related sensitivity, power consumption, and bandwidth have been analysed (Crescentini et al., 2017). Authors have analysed the devices by means of 3D-TCAD simulations embedding galvanomagnetic transport model, which takes into account the Lorentz force acting on carriers due to a magnetic field. For example, dimension of contacts in Hall sensors have been analysed through simulation. The Hall voltage at different points of the y-axis, on a device with sensing area of  $40 \mu\text{m} \times 40 \mu\text{m}$  has been measured and relevant curve has been produced. As it can be seen from Fig. 9A the spike on the  $y = 19.5 \mu\text{m}$  curve at about  $x = 20 \mu\text{m}$  is due to the presence of the highly doped contact while the oscillations relate to numerical errors. This study has exploited modern technology-computer-aided-design (TCAD) simulations to investigate the effects of design parameters on sensor performance. Simulations are based on Synopsis Sentaurus<sup>®</sup>, which implements galvanomagnetic transport mode, and are verified through experimental measurements on a prototype. Other simulation results have been defined a set of trade-offs and design rules that can be used by electronic designers to conceive their own Hall probes.

In another work authors have performed simulation to optimize the conductor structural parameters of a new free space current sensor using Ansoft Maxwell software. The optimized parameters are implemented in a free-space current sensor applying a Hall-effect element (Qiu et al., 2014). The goal of magnetic field simulation is to optimize the magnetic flux density that the Hall element senses under different conditions. Fig. 9B shows the simulation model, the main characteristics of which are as follows: a) Current excitation loads on the electric conductor. b) Adaptive meshing, the number of the elements is not more than 30,000. c) The nonlinear residual of the model is controlled within 0.01. The authors have concluded their studies as follows: a) The magnetic flux density generated by a U-shaped conductor is much higher than that by a straight conductor; b) A gap size of about 1.0 mm can guarantee the sensor to have an electrical isolation voltage of 2.5 kV.; c) A circular cross-section conductor is appreciated thanks to its low cost, easy availability and relatively high magnetic flux density generated by it.; d) The influence of the magnetic field generated by the part near the end of the conductor pins is gradually reduced by increasing length. e) The sensitivity of the new designed free-space current sensor is relatively stable and the average sensitivity is about 15 mV/A. f) The linearity error of the new designed free-space current sensor can be controlled within  $\pm 0.6\%$ . g) A basic accuracy of  $\pm 3.0\%$

is realizable for free-space current sensors under using the optimized parameters of the conductor.

#### 4.6. MR sensors

Tunnelling magnetoresistance (TMR) device has been used for *E. coli* detection by manipulating superparamagnetic beads to a sensing area (Li and Kosel, 2013). Instead of biochemical immobilization layer, which is commonly used in magnetic biosensor systems, in this work the trapping has been used. Replacing the biochemical immobilization layer by the trapping well greatly simplifies the detection process. A finite-element simulation is performed (using COMSOL software) to calculate  $B_M$ , the magnetic flux density generated by the current in the conducting line, and  $B_{\text{Stray}}$ , the magnetic flux density of magnetic beads inside the trapping well (Fig. 10A). The susceptibility of the superparamagnetic beads used is 0.79 (Dynabeads<sup>®</sup> M-270). In the model, the conducting line has a width of  $6 \mu\text{m}$ , a length of  $15 \mu\text{m}$  and a thickness of  $0.3 \mu\text{m}$ . The red rectangle in Fig. 10A represents the TMR sensor surface. It has a width of  $3 \mu\text{m}$ , a length of  $15 \mu\text{m}$  and zero thickness. The sensor surface is separated from the conducting line by a 200-nm thick layer of SiN and a 60-nm thick nonmagnetic top electrode of the TMR sensor. A direct current of 30 mA is applied to the conducting line in x-direction. The current creates a magnetic field, which changes the resistance of the TMR sensor. By whole device simulation of the bead in the corner of TMR (symmetry does not apply in this case), the average value of y component of  $B_{\text{Stray}}$  is calculated  $1.233\text{e-}2 \text{ mT}$ , corresponding to  $V_{\text{Stray}} = 155.9 \text{ nV}$ . For the bead in the centre of TMR, the average value of y component of  $B_{\text{Stray}}$  is obtained  $7.638\text{e-}3 \text{ mT}$ , and  $V_{\text{Stray}}$  is  $96.56 \text{ nV}$  (Fig. 10B and C). As expected, the output voltage of the TMR sensor caused by a single bead is the highest when the bead is located at the centre of the trapping well and is the lowest when the bead is located at its corner. The output voltage caused by a single bead should be between  $96.56 \text{ nV}$  (bead at a corner) and  $219.1 \text{ nV}$  (bead at the centre). This is in good agreement with the experimental results presented by authors in this study.

Following previous work, Li and Kosel (2014) have demonstrated the capability of TMR biosensor in the detection of *E. coli* (Fig. 10D and E). The trap is formed by a current-carrying microwire that attracts the magnetic beads into a sensing space on top of a TMR sensor. Fig. 10F shows the simulation results obtained for voltage,  $V_{\text{Stray}}$ , caused by an individual magnetic bead and its dependence on the bead's location. For one bead on the chip's surface at the centre of the micro-wire ( $Y = 0, Z = 1.4 \mu\text{m}$ )  $V_{\text{Stray}}$  is obtained  $87.52 \text{ nV}$ . This represents the highest value that can be expected from an individual bead. When the TMR sensor is fully covered with magnetic beads, two rows of magnetic beads in the first layer contribute the most to the total signal. When the bacteria are attached to the surface of the beads, a part of the sensing space will be

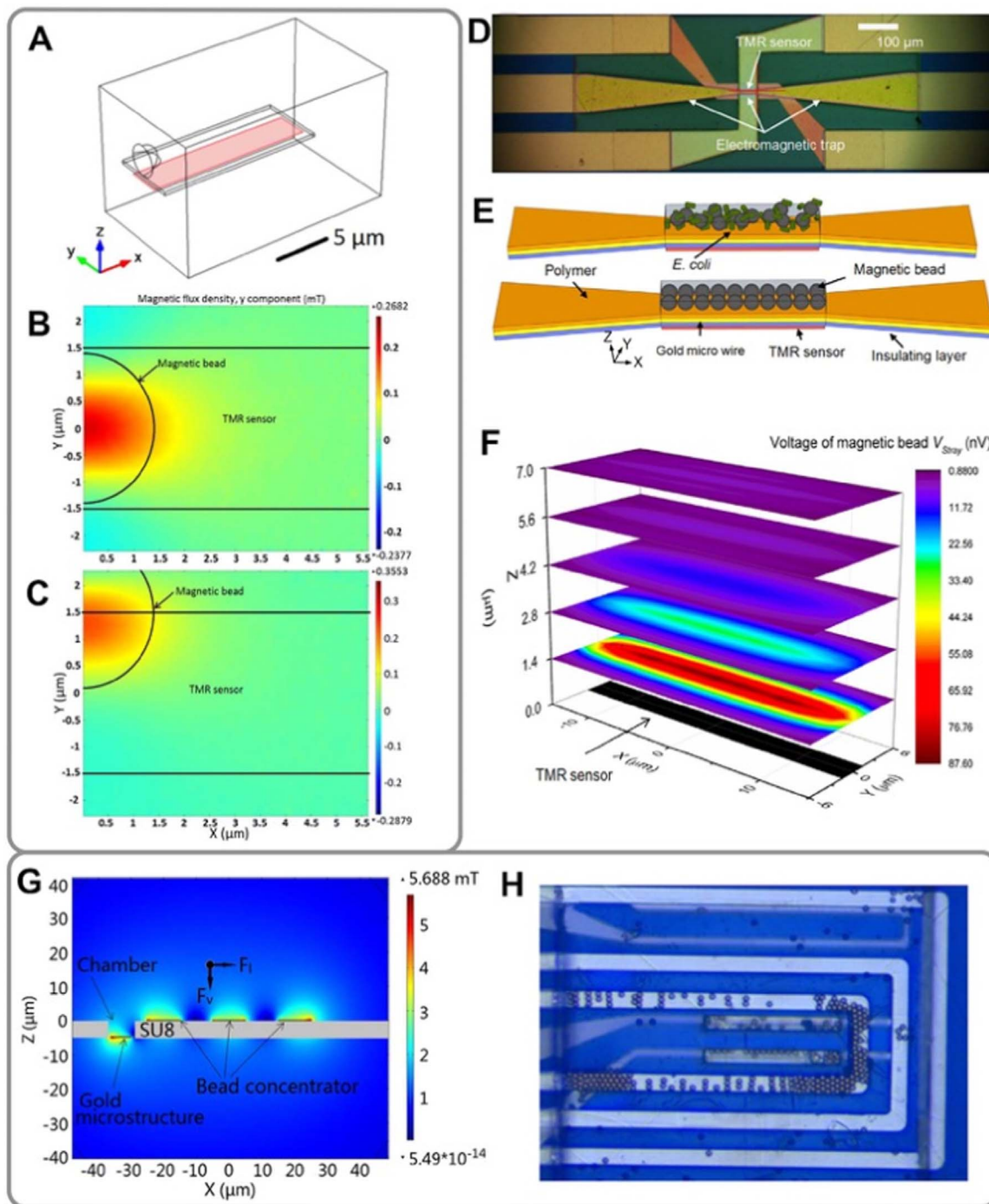


**Fig. 10.** (A) Model used for finite-element simulation of the effects of the magnetization current and superparamagnetic bead on the sensor. The red rectangle represents the TMR sensor's surface. The model also includes a bead and the conducting line. The sensitive direction of the TMR sensor is along the y-axis (Nabaei, 2014). Y-component of the flux density of a superparamagnetic bead magnetized by the current through the conductor at the sensor surface; (B) Bead at the centre of the sensor; (C) Bead at the edge of the sensor (Nabaei, 2014). A magnetic biosensor comprised of an electromagnetic trap and a tunnel magneto-resistive (TMR) sensor (Nabaei et al., 2013); (D) an optical image of the TMR biosensor. (E) Schematic of the detection method. The current in the microwire creates a non-uniform magnetic field, forming an electromagnetic trap on the top of the TMR biosensor. (F) Simulation results for the voltage of magnetic sensor caused by the stray field of an individual magnetic bead (Nabaei et al., 2013). (G) Magnitude of magnetic flux density and schematic cross-section of the device.  $F_l$  is the lateral magnetic force.  $F_v$  is the vertical magnetic force (Nazari Nejad, 2015). (H) Trapping of magnetic particles (Nazari Nejad, 2015). Reprinted with permissions. (For interpretation of the references to color in this figure legend, the reader is referred to the web version of this article).

occupied by them, yielding a decrease in the sensor signal. As one of the advantages of this technique and compared with magnetic biosensors previously developed by this group, it does not require surface bio-functionalization and procedure can be completed within half an hour. The same authors have used a bead concentrator, consisting of gold microstructures, at the bottom of a microchannel to attract and move magnetic particles into a trap (Li and Kosel, 2012). In this work, to

sense targets, two kinds of solutions have been arranged; one comprising only superparamagnetic particles, the other one containing beads with the protein bovine serum albumin as the target and fluorescent markers. Owing to the size difference between bare beads and beads with target, less magnetic beads were immobilized inside the volume chamber in case of magnetic beads with target as compared to bare magnetic beads. A simulation using commercial finite-element

software (COMSOL) is performed to calculate the magnetic field and magnetic force. The model as shown in Fig. 10G is the same to the fabricated device (Fig. 10H). The height of the gold microstructures is 300 nm. The current applied to the gold microstructure beneath the chamber is 30 mA. The other currents are increased to keep the same current density in all the gold microstructures. The height and width of the chamber made from SU8 is 5  $\mu\text{m}$  and 8  $\mu\text{m}$ , respectively. The magnetic bead has a diameter of 2.8  $\mu\text{m}$  and a magnetic susceptibility of 0.17, which are the values of a Dynabead M-270. Fig. 10G also shows the distribution of the magnetic field flux density. The strongest field exists near the gold microstructures. The field strength rapidly diminishes when moving away from the gold microstructures. The advantage of proposed method is that complex biological treatment of the sensor surface is not required, since a combination of magnetic forces and a mechanical trap is used to immobilize magnetic beads. The magnetic field generated by electrical currents can also be used to magnetize the magnetic beads. This eliminates the need for an external magnetic field source, which is commonly required for magnetoresistive biosensors. Another aspect worth to mention is that the concentrator would allow this system to operate on droplets rather than using microfluidic channels, which would reduce the complexity.

Micromagnetic simulation for detecting magnetic beads has been also performed by using a high-sensitivity spin-valve sensor as the detector in Liu et al. (2006). The magnetic beads polarized by a dc magnetic field contribute to a nonuniform dipole field, which can affect the magnetization state of spin-valve sensor, leading to a detectable resistance change (Fig. 11A–C). Magnetization configurations with six magnetic beads over the sense plane and that without the beads is shown in Fig. 11D, in a transverse 15 Oe applied field. The dipole field created by the magnetic beads is in the reversed direction which partially cancels the applied field, resulting in a small change of the magnetization of the free layer along the clockwise direction, which can be seen from the enlarged view, shown in Fig. 11F. Micromagnetic simulation study showed that single or several 2  $\mu\text{m}$  diam microbeads can be detected with about 98  $\mu\text{V}$  voltage change per bead, indicating that the single molecule detection with a micron-sized bead marker is possible. Nevertheless, single nano-sized bead as small as 250 nm shows low signal of about 34  $\mu\text{V}$ , which is hardly to be detected by using the present spin-valve sensors.

Li et al. (2003a) have fabricated a series of highly sensitive spin valve sensors on a micron scale that successfully detected the presence of a single superparamagnetic bead (Dynabeads M-280, 2.8  $\mu\text{m}$  in diameter) and thus showed suitability for identifying biomolecules labelled by such magnetic beads. By polarizing the magnetic microbead on a spin valve sensor with a dc magnetic field and modulating its magnetization with an orthogonal ac magnetic field, they observed a magnetoresistance (MR) signal reduction caused by the magnetic dipole field from the bead that partially cancelled the applied fields to the spin valve. A two-dimensional micromagnetic simulation for the spin valve sensors has been performed using the OOMMF software (Donahue et al., 1999). They have used OOMMF to simulate only the magnetization behaviour of the  $\text{Co}_{90}\text{Fe}_{10}$  free layer to obtain the corresponding MR responses. The saturation magnetization (1540  $\text{emu}/\text{cm}^3$ ) and exchange stiffness (1.53  $\mu\text{erg}/\text{cm}$ ) of  $\text{Co}_{90}\text{Fe}_{10}$  were obtained from Williams (2001). The uniaxial anisotropy field was found to be 40 Oe, close to the reference value of 32 Oe (Pratt et al., 1991). The cell size was chosen to be 25 nm for the micron-sized sensors. The Dynabeads are considered as a magnetic dipole, and their susceptibility was experimentally found to be  $\sim 0.04$ . The resistance changes  $\Delta\tilde{R}_{\text{sen,simu}}$  from simulations is presented in Table 2. It can be seen that the simulations are consistent with the measurements. Further experiments and showed that these sensors or their variations can detect 1–10 Co nanoparticles with a diameter of about 11 nm, and are suitable for DNA fragment detection.

Li et al. (2014) have presented an external field-free magnetic bio sensing structure, which will be useful for magnetic bio sensing system

miniaturization. This structure is based on unique patterned grooves embedded in spin valve biosensor and employs the stray fields from the free and pinned layers of biosensor for magnetic nanoparticle (MNP) magnetization. Micromagnetic simulation has been carried out using OOMMF software (Donahue, 1999), to simulate the magnetization behaviour of the free layer under the stray field from the pinned layer and the dipole field from the MNPs. In the simulation, both the free and pinned layer with a groove structure are divided into small magnetic cells with the same size (5 nm). Each magnetic cell has its own magnetic moment and interacts with all other cells. Before the MNP bonding, the effective field on the free layer is the sum of the stray field from all the magnetic cells of the pinned layer. The MNP is magnetized by the total field from all the magnetic cells of the free and pinned layers. The dipole field from the MNP is discretized and incorporated into the OOMMF input file as well as the stray field from the pinned layer on the free layer. The averaged magnetization orientations of the free layer are computed from the magnetization distribution of the magnetic cells by OOMMF. Results showed a maximum signal to noise ratio of 18.6 dB from one 8 nm radius iron oxide magnetic nanoparticle locating in the centre of the groove structure and the signal strength increased with the MNP position near the groove corner.

In another work Wirix-Speetjens et al. (2006) have described a detection system based on a magnetic spin-valve sensor that is capable of giving position-time information of the magnetic behaviour of one single bead. The results obtained with this system for the detection of a single particle signature are then compared with simulations. For this comparison, they have developed a model where an additional particle-substrate separation distance is included. This distance is determined by a force balance of the perpendicular forces acting on the magnetic particle, including the magnetic and electrostatic force. As it can be seen from Fig. 11K, these simulations agree well with the single particle detection experiment. A finite element analysis using Maxwell 3D from Ansoft has been applied for the simulations. This tool requires the value of the relative permeability of the particle's material. This relative permeability is obtained by measuring the magnetic susceptibility, which is related to it, using a SQUID of quantum design. From the SQUID data, a value of  $\chi=0.257 \pm 0.015$  for the susceptibility, and incorporating the particle's demagnetization field, a value of  $1.28 \pm 0.02$  for the relative permeability has been obtained (O'handley, 2000). The model illustrated the importance of the additional particle/substrate separation distance, which was found to be 1250 nm for their particle detection system. When this separation distance is not taken into account, the peak to peak signal increases from 250 to about 800  $\mu\text{V}$ . Authors have concluded that this additional separation distance is an important parameter and needs to be taken into account for modelling the sensor response of unbound particles.

#### 4.7. Superconducting quantum interference device (SQUID)

Authors have striven to clarify the mechanism of weakness in magnetic noise by means of numerical electromagnetic field simulation to support a SQUID development (Terauchi et al., 2014). A non-linear current-voltage characteristic of the Josephson junction is taken into account the simulation to represent the SQUID behaviour. As the results, the phenomena of the step-increasing magnetic flux and the spike voltage is simulated. The simplified non-linear current-voltage characteristic of the Josephson junction is considered in the developed simulation using the 3-D finite element method (FEM) (Terauchi et al., 2012). The simulation model includes the dc-SQUID ring with two Josephson junctions and the around air region. The bias current of 10.0  $\mu\text{A}$  flows into the dc-SQUID ring. The critical current of the Josephson junction is 7.0  $\mu\text{A}$ . In the simulation, an external magnetic field is applied parallel to the z-axis and uniformly increases from 0 to 5.0  $\mu\text{T}$ . In order to investigate the electromagnetic behaviour of the dc-SQUID ring, the magnetic flux crossing the dc-SQUID ring and the voltage between the terminals of the dc-SQUID ring are computed.

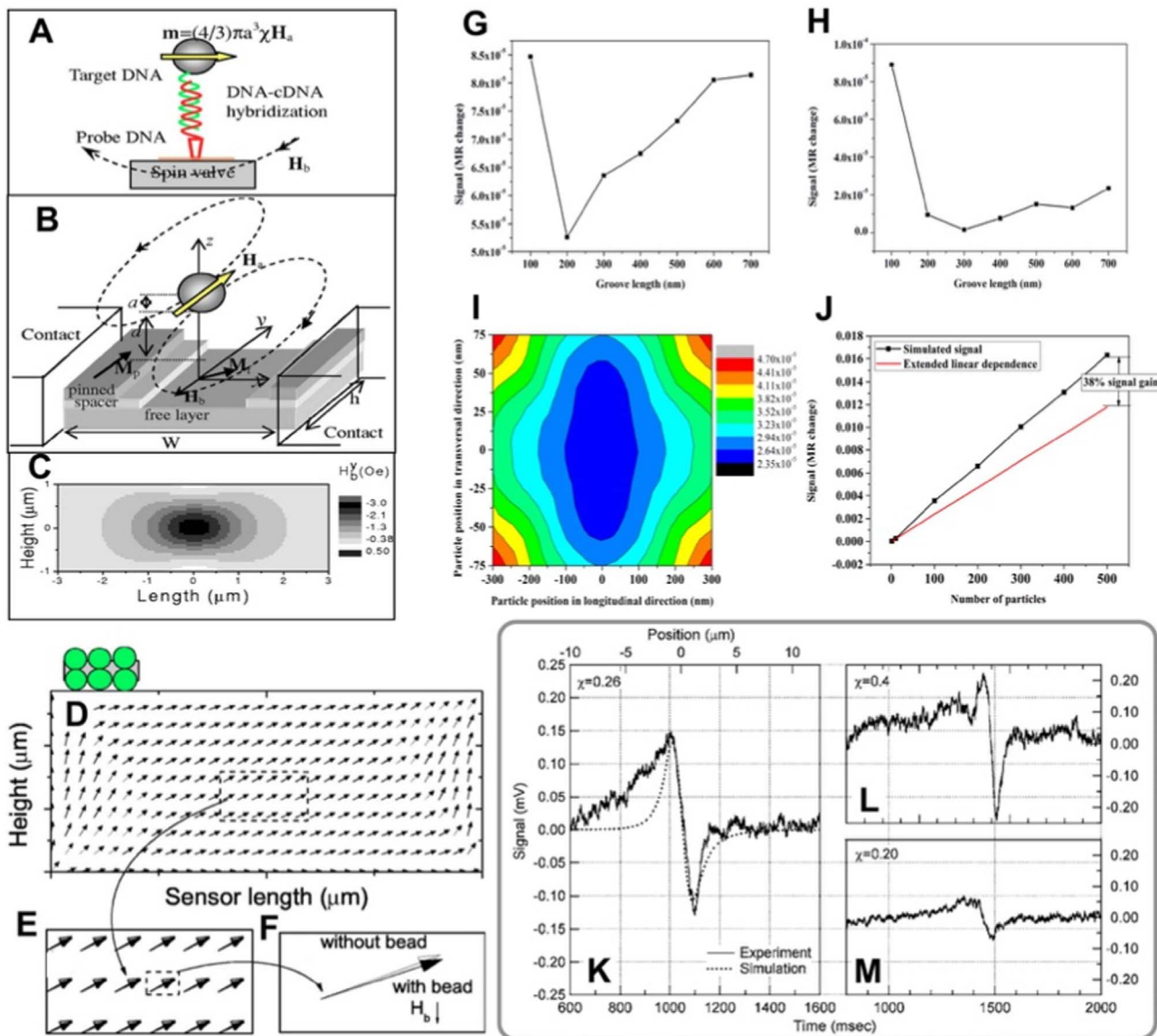


Fig. 11. (A) Schematic diagram of the MR biosensor based on the molecular recognition of DNA hybridization. (B) Illustration of the spin-valve sensor and magnetic bead, the magnetization configuration, applied field  $H_a$  and dipole field  $H_b$  are also sketched. (C) Calculated dipole field distribution for a 2  $\mu\text{m}$  diam microbead (O’handley, 2000). (D) Simulated magnetization configuration of free layer with six magnetic beads (solid dark arrows) and that without beads (open gray arrows). The beads are located in a uniform array over the sense plane (O’handley, 2000). (E) and (F) are the corresponding enlarged views. The dipole field direction is sketched in the plot of (F) (O’handley, 2000). (G) The signal from one 8 nm radius iron oxide magnetic nanoparticle, in terms of MR change, of biosensor with 100 nm groove width and different groove length (Pratt et al., 1991). (H) The signal from one 8 nm radius iron oxide magnetic nanoparticle, in terms of MR change, of biosensor with 200 nm groove width and different groove length. (I) Signal dependence on the particle position inside the groove structure, in terms of MR change, of biosensor with 200 nm groove width (transversal direction) and 700 nm groove length (longitudinal direction). (J) The signal dependence on the particle number, in terms of MR change, of biosensor with 200 nm groove width and 700 nm groove length. The black dotted curve is the simulation result and the red curve is the extended linear dependence from one particle signal (Pratt et al., 1991). (K) Simulated (dotted line) and experimental data (solid line) showing the sensor response when a single magnetic particle with an average susceptibility crosses the sensor (Prinz, 1998). (L) and (M) show the sensor response when a particle with either a high or low susceptibility is transported across the sensor (Prinz, 1998). Reprinted with permissions.

Fig. 12 shows the current density distribution on the superconducting and voltage states, respectively. On Fig. 12A, the current disproportionately flows in the Josephson junctions. On the other hand, the less current flows on Fig. 12B. When the Josephson junction is assumed as a constant resistance, these phenomena, the step-increasing

magnetic flux and the spike voltage, cannot be reproduced. It is successful to realize the qualitative expression of the SQUID behaviour by taking into account the current-voltage characteristic of the Josephson junction. For further study, the more elaborate consideration of the Josephson junction is required for quantitative evaluation. For

Table 2

Experimental data for two spin valve sensors with a single 2.8 mm diam magnetic bead (Dynabeads M-280) and the micromagnetic simulation results. The voltages are all rms values.

Sensor size ( $\mu\text{m}^2$ )	Active area ( $\mu\text{m}^2$ )	$H_t$ (Oe rms)	$H_b$ (Oe)	$V_{bias}$ (V)	$R_2/R_1$ (k $\Omega$ / k $\Omega$ )	$V_{sig}^0/V_{noise}$ (mV/mV)	$V_{sig}/V_{noise}$ (mV/mV)	$\Delta\hat{R}_{sen}$ (m $\Omega$ )	$\Delta\hat{R}_{sen,sim}$ (m $\Omega$ )
3 × 12	3 × 4.1	32.0	120.0	30.0	9.13/9.53	0.03/0.09	1.2/0.1	5.2	5.6
2.5 × 10	2.5 × 3.8	38.0	94.0	100.0	22.2/24.8	0.04/0.15	3.8/0.3	11.9	13.3

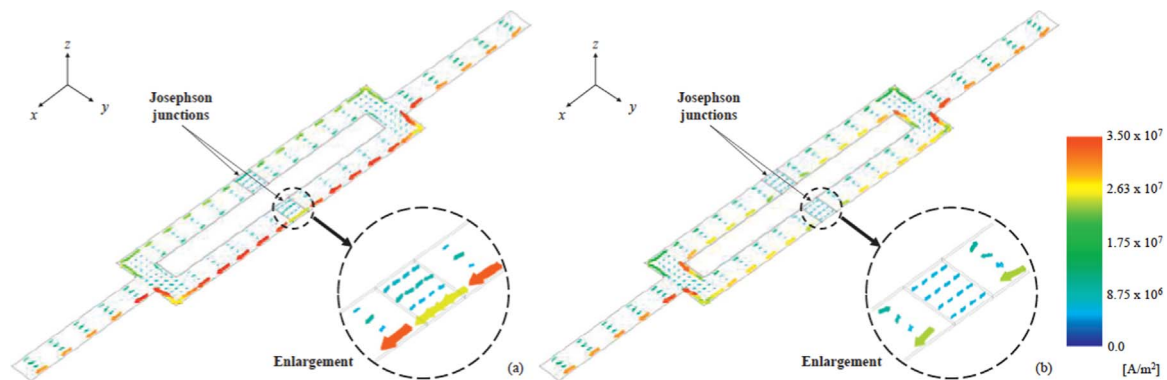


Fig. 12. Current density distribution on (A) Superconducting state and (B) Voltage state.

example, a phase difference across the Josephson junction is not considered yet.

## 5. Conclusions and future perspectives

It is evident that magnetic biosensor computational models developed so far are mostly restricted to the simulation in commercial Multiphysics modelling software. Despite numerous attempts, there have been only few numbers of works on developing a comprehensive and multi-aspect model based in-house modelling approach. Such an in-house model is advantageous to the models developed in commercial Multiphysics software, because of its high flexibilities in introducing various states and working conditions as well as high capability to be modified and extended for simulation of a range of complex problems and applications. In contrary, creating an in-house model is an exhaustive work and has some challenges that developer(s) might encounter. Developing a comprehensive and validated custom software are often beyond the abilities of an individual or even a team that may deliver a product full of bugs and other issues. For example, to develop a numerical model for an engineering problem, it requires to perform problem formulation (mathematical model development), and then apply a proper and suitable discretization technique (such as Fine Element Method, Finite Difference Method, and Boundary Element Method), considering the type of the problem. Debugging, and time-consuming calculations (because of high number of meshes) are the other challenges in this procedure. Developer(s) can overcome these challenges, using latest techniques accomplished in different engineering sciences (e.g. new technologies in computer science, such as General-purpose Computing on Graphics Processing Units (GPGPU)).

Future perspective of magnetic biosensors and their design techniques and methodologies will be dramatically influenced by progresses in different fields of research. Current advancements in bionanotechnology, computer science, materials engineering and molecular diagnostics, coupled with increasing demands for miniaturized medical devices for portable, wearable and implantable applications will trigger research efforts to develop advanced technologies for fabrication of miniaturized, highly sensitive, fast, reliable, cost-effective, easy-to-use magnetic biosensors. This generation transformation which can meet future medical devices needs is a challenging process. The role of computational modelling and simulation cannot be ignored and are critical to push technologies towards achieving large scale applications and impact.

## Acknowledgment

R.C. acknowledges the support from the Australian Research Council Discovery Early Career Researcher Award (ARC DECRA DE170100068).

## References

- Albon, C., Weddemann, A., Auge, A., Rott, K., Hütten, A., 2009. Tunneling magnetoresistance sensors for high resolution particle detection. *Appl. Phys. Lett.* 95 (2), 023101.
- Aledeat, K., Mihajlović, G., Chen, K., Field, M., Sullivan, G.J., Xiong, P., Chase, P.B., von Molnar, S., 2010. Dynamic micro-Hall detection of superparamagnetic beads in a microfluidic channel. *J. Magn. Magn. Mater.* 322 (24), L69–L72.
- Baibich, M.N., Broto, J.M., Fert, A., Vandau, F.N., Petroff, F., Eitenne, P., Creuzet, G., Friederich, A., Chazelas, J., 1988. Giant magnetoresistance of (001)Fe/(001)Cr magnetic superlattices. *Phys. Rev. Lett.* 61 (21), 2472–2475.
- Barbolina, I., Novoselov, K., Morozov, S., Dubonos, S., Missous, M., Volkov, A., Christian, D., Grigorieva, I., Geim, A., 2006. Submicron sensors of local electric field with single-electron resolution at room temperature. *Appl. Phys. Lett.* 88 (1), 013901.
- Baselt, D.R., Lee, G.U., Natesan, M., Metzger, S.W., Sheehan, P.E., Colton, R.J., 1998. A biosensor based on magnetoresistance technology. *Biosens. Bioelectron.* 13 (7), 731–739.
- Baumgartner, A., Ihn, T., Ensslin, K., Papp, G., Peeters, F., Maranowski, K., Gossard, A., 2006. Classical Hall effect in scanning gate experiments. *Phys. Rev. B* 74 (16), 165426.
- Beguivin, A., Corte-León, H., Manzin, A., Nabaei, V., Krzysteczko, P., Schumacher, H.W., Petit, D., Cowburn, R.P., Kazakova, O., 2014. Simultaneous magnetoresistance and magneto-optical measurements of domain wall properties in nanodevices. *J. Appl. Phys.* 115 (17), 17C718.
- Besse, P.A., Boero, G., Demierre, M., Pott, V., Popovic, R., 2002. Detection of a single magnetic microbead using a miniaturized silicon Hall sensor. *Appl. Phys. Lett.* 80 (22), 4199–4201.
- Binasch, G., Grunberg, P., Saurenbach, F., Zinn, W., 1989. Enhanced magnetoresistance in layered magnetic-structures with antiferromagnetic interlayer exchange. *Phys. Rev. B* 39 (7), 4828–4830.
- Birla, R., 2016. *Biosensors in Tissue and Organ Fabrication*. Springer International Publishing.
- Blohm, D.H., Guiseppi-Elie, A., 2001. New developments in microarray technology. *Curr. Opin. Biotechnol.* 12 (1), 41–47.
- Brzeska, M., Panhorst, M., Kamp, P.B., Schotter, J., Reiss, G., Puhler, A., Becker, A., Bruckl, H., 2004. Detection and manipulation of biomolecules by magnetic carriers. *J. Biotechnol.* 112 (1–2), 25–33.
- Chin, C.D., Linder, V., Sia, S.K., 2007. Lab-on-a-chip devices for global health: past studies and future opportunities. *Lab Chip* 7 (1), 41–57.
- Christoph, V., Wirth, S., von Molnár, S., 2001. Magnetic measurements and numerical simulations of interacting nanometer-scale particles. *J. Appl. Phys.* 89 (11), 7472–7474.
- Cobas, E., Friedman, A.L., van't Erve, O.M.J., Robinson, J.T., Jonker, B.T., 2012. Graphene as a tunnel barrier: graphene-based magnetic tunnel junctions. *Nano Lett.* 12 (6), 3000–3004.
- Colle, F., 2008. *Hall Sensor Based Detection of Magnetic Particles for Lab-on-a-Chip*. GENT University.
- Corte-León, H., Nabaei, V., Manzin, A., Fletcher, J., Krzysteczko, P., Krzysteczko, H.W., Kazakova, O., 2014. Anisotropic magnetoresistance state space of permalloy nanowires with domain wall pinning geometry. *Sci. Rep.* 4.
- Costa, T., Cardoso, F.A., Germano, J., Freitas, P.P., Piedade, M.S., 2017. A CMOS front-end with integrated magnetoresistive sensors for biomolecular recognition detection applications. *IEEE Trans. Biomed. Circuits Syst.* 11 (5), 988–1000.
- Cowburn, R.P., Koltsov, D.K., Adeyeye, A.O., Welland, M.E., Tricker, D.M., 1999. Single-domain circular nanomagnets. *Phys. Rev. Lett.* 83 (5), 1042–1045.
- Crescentini, M., Biondi, M., Romani, A., Tartagni, M., Sangiorgi, E., 2017. Optimum design rules for CMOS hall sensors. *Sensors* 17 (4), 765.
- Di Michele, L., Shelly, C., Gallop, J., Kazakova, O., 2010. Single particle detection: phase control in submicron Hall sensors. *J. Appl. Phys.* 108, 10.
- Di Michele, L., Shelly, C., de Marco, P., See, P., Cox, D., Kazakova, O., 2011. Detection and susceptibility measurements of a single Dynal bead. *J. Appl. Phys.* 110, 6.
- Dieny, B., Speriosu, V.S., Parkin, S.S., Gurney, B.A., Wilhoit, D.R., Mauri, D., 1991. Giant magnetoresistive in soft ferromagnetic multilayers. *Phys. Rev. B* 43 (1), 1297.
- Donahue, M., Porter, D., Lau, J., McMichael, R., Donahue, M., 1999. *Interagency Report*



- NISTIR 6376. NIST J. Res. National Institute of Standards and Technology, Gaithersburg, vol. 114, pp. 57–67.
- Donahue, M.J., 1999. OOMMF User's Guide, Version 1.0. -6376.
- Donolato, M., Gobbi, M., Vavassori, P., Leone, M., Cantoni, M., Metlushko, V., Ilic, B., Zhang, M., Wang, S.X., Bertacco, R., 2009. Nanosized corners for trapping and detecting magnetic nanoparticles. *Nanotechnology* 20 (38), 385501.
- Donolato, M., Vavassori, P., Gobbi, M., Deryabina, M., Hansen, M.F., Metlushko, V., Ilic, B., Cantoni, M., Petti, D., Brivio, S., Bertacco, R., 2010. On-chip manipulation of protein-coated magnetic beads via domain-wall conduits. *Adv. Mater.* 22 (24), 2706.
- Ennen, I., Kappe, D., Rempel, T., Glenske, C., Hütten, A., 2016. Giant magnetoresistance: basic concepts, microstructure, magnetic interactions and applications. *Sensors* 16 (6), 904.
- Enpuku, K., Inoue, K., Soejima, K., Yoshinaga, K., Kuma, H., Hamasaki, N., 2005. Magnetic immunoassays utilizing magnetic markers and a high-T/sub c/SQUID. *IEEE Trans. Appl. Supercond.* 15 (2), 660–663.
- Enserink, M., 2001. Biodefense hampered by inadequate tests. *Science* 294 (5545), 1266–1267.
- Folks, L., Troup, A., Boone, T., Katine, J., Nishioka, M., Grobis, M., Sullivan, G., Ikhlassi, A., Field, M., Gurney, B., 2009. Near-surface nanoscale InAs Hall cross sensitivity to localized magnetic and electric fields. *J. Phys.: Condens. Matter* 21 (25), 255802.
- Gallagher, W.J., Parkin, S.S.P., Lu, Y., Bian, X.P., Marley, A., Roche, K.P., Altman, R.A., Rishton, S.A., Jahnes, C., Shaw, T.M., Xiao, G., 1997. Microstructured magnetic tunnel junctions. *J. Appl. Phys.* 81 (8), 3741–3746.
- Gijs, M.A.M., 2004. Magnetic bead handling on-chip: new opportunities for analytical applications. *Microfluid. Nanofluid.* 1 (1), 22–40.
- Gomez, R.D., Luu, T.V., Pak, A.O., Kirk, K.J., Chapman, J.N., 1999. Domain configurations of nanostructured permalloy elements. *J. Appl. Phys.* 85 (8), 6163–6165.
- Graham, D.L., Ferreira, H.A., Freitas, P.P., 2004. Magnetoresistive-based biosensors and biochips. *Trends Biotechnol.* 22 (9), 455–462.
- Graham, D.L., Ferreira, H.A., Feliciano, N., Freitas, P.P., Clarke, L.A., Amaral, M.D., 2005. Magnetic field-assisted DNA hybridisation and simultaneous detection using micron-sized spin-valve sensors and magnetic nanoparticles. *Sens. Actuators B Chem.* 107 (2), 936–944.
- Guslienko, K.Y., Novosad, V., Otani, Y., Shima, H., Fukamichi, K., 2002. Magnetization reversal due to vortex nucleation, displacement, and annihilation in submicron ferromagnetic dot arrays. *Phys. Rev. B* 65, 2.
- Haun, J.B., Devaraj, N.K., Hilderbrand, S.A., Lee, H., Weissleder, R., 2010. Bioorthogonal chemistry amplifies nanoparticle binding and enhances the sensitivity of cell detection. *Nat. Nanotechnol.* 5 (9), 660–665.
- Heidari, H., Bonizzoni, E., Gatti, U., Maloberti, F., 2014. A current-mode CMOS integrated microsystem for current spinning magnetic Hall sensors. *IEEE Int. Symp. Circuits Syst.* 678–681.
- Heidari, H., Bonizzoni, E., Gatti, U., Maloberti, F., 2015. A CMOS current-mode magnetic Hall sensor With integrated front-end. *IEEE Trans. Circuits Syst. I Regul. Pap.* 62 (5), 1270–1278.
- Heidari, H., Bonizzoni, E., Gatti, U., Maloberti, F., Dahiya, R., 2016. CMOS vertical Hall magnetic sensors on flexible substrate. *IEEE Sens. J.* 16 (24), 8736–8743.
- Heidari, H., Gatti, U., Bonizzoni, E., Maloberti, F., 2013. Low-Noise Low-Offset Current-Mode Hall Sensors. In: *Proceedings of the IEEE Conference on Ph.D. Research in Microelectronics and Electronics (PRIME)*, pp. 325–328.
- Hengstmann, T.M., Grundler, D., Heyn, C., Heitmann, D., 2001. Stray-field investigation on permalloy nanodisks. *J. Appl. Phys.* 90 (12), 6542–6544.
- Huang, C.-C., Zhou, X., Hall, D.A., 2017. Giant magnetoresistive biosensors for time-domain magnetorelaxometry: a theoretical investigation and progress toward an immunoassay. *Sci. Rep.* 7.
- Issadore, D., Chung, H.J., Chung, J., Budin, G., Weissleder, R., Lee, H., 2013.  $\mu$ Hall chip for sensitive detection of bacteria. *Adv. Healthc. Mater.* 2 (9), 1224–1228.
- Kazakova, O., Gallop, J., Perkins, G., Cohen, L., 2007. Scanned micro-Hall microscope for detection of biofunctionalized magnetic beads. *Appl. Phys. Lett.* 90 (16).
- Kazakova, O., Panchal, V., Gallop, J., See, P., Cox, D.C., Spasova, M., Cohen, L.F., 2010. Ultrasmall particle detection using a submicron Hall sensor. *J. Appl. Phys.* 107, 9.
- Khan, M., Henk, J., Bruno, P., 2008. Anisotropic magnetoresistance in Fe/MgO/Fe tunnel junctions. *J. Phys.: Condens. Matter* 20 (15), 155208.
- Kim, K.W., Reddy, V., Torati, S.R., Hu, X.H., Sandhu, A., Kim, C.G., 2015. On-chip magnetometer for characterization of superparamagnetic nanoparticles. *Lab Chip* 15 (3), 696–703.
- Kirk, K.J., Chapman, J.N., Wilkinson, C.D.W., 1997. Switching fields and magnetostatic interactions of thin film magnetic nanoelements. *Appl. Phys. Lett.* 71 (4), 539–541.
- Koh, I., Josephson, L., 2009. Magnetic nanoparticle sensors. *Sensors* 9 (10), 8130–8145.
- Kotitz, R., Matz, H., Trahms, L., Koch, H., Weitschies, W., Rheinlander, T., Semmler, W., Bunte, T., 1997. SQUID based remanence measurements for immunoassays. *IEEE Trans. Appl. Supercond.* 7 (2), 3678–3681.
- Krause, H.J., Kreutzbruck, M.V., 2002. Recent developments in SQUID NDE. *Phys. C: Supercond.* 368 (1), 70–79.
- Krishna, V.D., Wu, K., Perez, A.M., Wang, J.-P., 2016. Giant Magnetoresistance-based biosensor for detection of influenza A virus. *Front. Microbiol.* 7.
- Kumagai, Y., Imai, Y., Abe, M., Sakamoto, S., Handa, H., Sandhu, A., 2008. Sensitivity dependence of Hall biosensor arrays with the position of superparamagnetic beads on their active regions. *J. Appl. Phys.* 103 (7), 07A309.
- Landry, G., Miller, M.M., Bennett, B.R., Johnson, M., Smolyaninova, V., 2004. Characterization of single magnetic particles with InAs quantum-well Hall devices. *Appl. Phys. Lett.* 85 (20), 4693–4695.
- Lee, W., Joo, S., Kim, S.U., Rhie, K., Hong, J., Shin, K.-H., Kim, K.H., 2009. Magnetic bead counter using a micro-Hall sensor for biological applications. *Appl. Phys. Lett.* 94 (15), 153903.
- Lenz, J., Edelstein, S., 2006. Magnetic sensors and their applications. *IEEE Sens. J.* 6 (3), 631–649.
- Lenz, J.E., 1990. A review of magnetic sensors. *Proc. IEEE* 78 (6), 973–989.
- Li, F., Kosel, J., 2012. A magnetic method to concentrate and trap biological targets. *IEEE Trans. Magn.* 48 (11), 2854–2856.
- Li, F., Kosel, J., 2013. A magnetic biosensor system for detection of E. coli. *IEEE Trans. Magn.* 49 (7), 3492–3495.
- Li, F., Kosel, J., 2014. An efficient biosensor made of an electromagnetic trap and a magneto-resistive sensor. *Biosens. Bioelectron.* 59, 145–150.
- Li, G., Joshi, V., White, R.L., Wang, S.X., Kemp, J.T., Webb, C., Davis, R.W., Sun, S., 2003a. Detection of single micron-sized magnetic bead and magnetic nanoparticles using spin valve sensors for biological applications. *J. Appl. Phys.* 93 (10), 7557–7559.
- Li, G.X., Joshi, V., White, R.L., Wang, S.X., Kemp, J.T., Webb, C., Davis, R.W., Sun, S.H., 2003b. Detection of single micron-sized magnetic bead and magnetic nanoparticles using spin valve sensors for biological applications. *J. Appl. Phys.* 93 (10), 7557–7559.
- Li, G.X., Sun, S.H., Wilson, R.J., White, R.L., Pourmand, N., Wang, S.X., 2006. Spin valve sensors for ultrasensitive detection of superparamagnetic nanoparticles for biological applications. *Sens. Actuators A Phys.* 126 (1), 98–106.
- Li, Y., Srinivasan, B., Jing, Y., Yao, X., Hugger, M.A., Wang, J.-P., Xing, C., 2010. Nanomagnetic competition assay for low-abundance protein biomarker quantification in unprocessed human sera. *J. Am. Chem. Soc.* 132 (12), 4388–4392.
- Li, Y., Wang, Y., Klein, T., Wang, J.-P., 2014. External-field-free magnetic biosensor. *Appl. Phys. Lett.* 104 (12), 122401.
- Li, Z., De Groot, C., Moodera, J.H., 2000. Gallium oxide as an insulating barrier for spin-dependent tunneling junctions. *Appl. Phys. Lett.* 77 (22), 3630–3632.
- Liu, Y., Jin, W., Yang, Y., Wang, Z., 2006. Micromagnetic simulation for detection of a single magnetic microbead or nanobead by spin-valve sensors. *J. Appl. Phys.* 99 (8), 08G102.
- Llano, J., Hayward, T., Morecroft, D., Bland, J., Castaño, F., Colin, I., Ross, C., 2007. Quantitative digital detection of magnetic beads using pseudo-spin-valve rings for multiplexed bioassays. *Appl. Phys. Lett.* 91 (20), 203904.
- Llano, J., Palfreyman, J.J., Ionescu, A., Barnes, C.H.W., 2010. Magnetic biosensor technologies for medical applications: a review. *Med. Biol. Eng. Comput.* 48 (10), 977–998.
- Manandhar, P., Chen, K.S., Aledeat, K., Mihajlovic, G., Yun, C.S., Field, M., Sullivan, G.J., Strouse, G.F., Chase, P.B., von Molnar, S., Xiong, P., 2009. The detection of specific biomolecular interactions with micro-Hall magnetic sensors. *Nanotechnology* 20 (35).
- Manzin, A., Nabaei, V., 2014. Modelling of micro-Hall sensors for magnetization imaging. *J. Appl. Phys.* 115 (17), 17E506.
- Manzin, A., Nabaei, V., Kazakova, O., 2012. Modelling and optimization of submicron Hall sensors for the detection of superparamagnetic beads. *J. Appl. Phys.* 111 (7), 07E513.
- Manzin, A., Nabaei, V., Corte-León, H., Kazakova, O., Krzyszczyk, P., Schumacher, H.W., 2014. Modeling of anisotropic magnetoresistance properties of permalloy nanostructures. *IEEE Trans. Magn.* 50 (4), 1–4.
- McGuire, T.R., Potter, R.I., 1975. Anisotropic magnetoresistance in ferromagnetic 3d alloys. *IEEE Trans. Magn.* 11 (4), 1018–1038.
- Mihajlovic, G., Xiong, P., von Molnar, S., Ohtani, K., Ohno, H., Field, M., Sullivan, G.J., 2005. Detection of single magnetic bead for biological applications using an InAs quantum-well micro-Hall sensor. *Appl. Phys. Lett.* 87 (11).
- Mihajlovic, G., Aledeat, K., Xiong, P., Von Molnar, S., Field, M., Sullivan, G.J., 2007. Magnetic characterization of a single superparamagnetic bead by phase-sensitive micro-Hall magnetometry. *Appl. Phys. Lett.* 91 (17).
- Miller, M.M., Prinz, G.A., Cheng, S.F., Bounnak, S., 2002. Detection of a micron-sized magnetic sphere using a ring-shaped anisotropic magnetoresistance-based sensor: a model for a magnetoresistance-based biosensor. *Appl. Phys. Lett.* 81 (12), 2211–2213.
- Miyazaki, T., Tezuka, N., 1995. Giant magnetic tunneling effect in Fe/Al<sub>2</sub>O<sub>3</sub>/Fe junction. *J. Magn. Magn. Mater.* 139 (3), L231–L234.
- Moodera, J.S., Kinder, L.R., Wong, T.M., Meservey, R., 1995. Large magnetoresistance at room temperature in ferromagnetic thin film tunnel junctions. *Phys. Rev. Lett.* 74 (16), 3273.
- Moura-Melo, W.A., Pereira, A.R., Silva, R.L., Oliveira, N.M., 2008. How hole defects modify vortex dynamics in ferromagnetic nanodisks. *J. Appl. Phys.* 103, 12.
- Munoz-Rojas, F., Fernandez-Rossier, J., Palacios, J.J., 2009. Giant magnetoresistance in ultrasmall graphene based devices. *Phys. Rev. Lett.* 102, 13.
- Nabaei, V., 2014. Modelling of Nanostructured Devices for Magnetic Sensing Applications. Polytechnic University of Turin.
- Nabaei, V., Rajkumar, R., Manzin, A., Kazakova, O., Tzalenchuk, A., 2013. Optimization of Hall bar response to localized magnetic and electric fields. *J. Appl. Phys.* 113 (6), 064504.
- Nazari Nejad, S., 2015. *Miniature Magnetic Sensors*.
- O'handley, R.C., 2000. *Modern Magnetic Materials: Principles and Applications*. Wiley.
- Pankhurst, Q.A., Connolly, J., Jones, S.K., Dobson, J., 2003. Applications of magnetic nanoparticles in biomedicine. *J. Phys. D: Appl. Phys.* 36 (13), R167–R181.
- Parkin, S.S.P., Kaiser, C., Panchula, A., Rice, P.M., Hughes, B., Samant, M., Yang, S.-H., 2004a. Giant tunnelling magnetoresistance at room temperature with MgO (100) tunnel barriers. *Nat. Mater.* 3 (12), 862–867.
- Parkin, S.S.P., Kaiser, C., Panchula, A., Rice, P.M., Hughes, B., Samant, M., Yang, S.H., 2004b. Giant tunnelling magnetoresistance at room temperature with MgO (100) tunnel barriers. *Nat. Mater.* 3 (12), 862–867.
- Pratt, W.P., Lee, S.F., Slaughter, J.M., Loloee, R., Schroeder, P.A., Bass, J., 1991. Perpendicular giant magnetoresistances of Ag/Co multilayers. *Phys. Rev. Lett.* 66 (23), 3060–3063.

- Prejbeanu, I.L., Natali, M., Buda, L.D., Ebels, U., Lebib, A., Chen, Y., Ounadjela, K., 2002. In-plane reversal mechanisms in circular Co dots. *J. Appl. Phys.* 91 (10), 7343–7345.
- Prinz, G.A., 1998. Magneto-electronics. *Science* 282 (5394), 1660–1663.
- Pulwey, R., Rahm, M., Biberger, J., Weiss, D., 2001. Switching behavior of vortex structures in nanodisks. *Ieee Trans. Magn.* 37 (4), 2076–2078.
- Qiu, J., Liu, J.-G., Zhang, Q., Lin, J., 2014. Simulation and optimization of conductor structural parameters of free-space hall-effect current sensor. In: *Proceedings of the 2014 IEEE International Workshop on Applied Measurements for Power Systems Proceedings (AMPS)*, pp. 1–6.
- Raabe, J., Pulwey, R., Sattler, R., Schweinbock, T., Zweck, J., Weiss, D., 2000. Magnetization pattern of ferromagnetic nanodisks. *J. Appl. Phys.* 88 (7), 4437–4439.
- Rahm, M., Biberger, J., Umansky, V., Weiss, D., 2003a. Vortex pinning at individual defects in magnetic nanodisks. *J. Appl. Phys.* 93 (10), 7429–7431.
- Rahm, M., Schneider, M., Biberger, J., Pulwey, R., Zweck, J., Weiss, D., Umansky, V., 2003b. Vortex nucleation in submicrometer ferromagnetic disks. *Appl. Phys. Lett.* 82 (23), 4110–4112.
- Rahm, M., Hollinger, R., Umansky, V., Weiss, D., 2004a. Influence of point defects on magnetic vortex structures. *J. Appl. Phys.* 95 (11), 6708–6710.
- Rahm, M., Stahl, J., Wegscheider, W., Weiss, D., 2004b. Multistable switching due to magnetic vortices pinned at artificial pinning sites. *Appl. Phys. Lett.* 85 (9), 1553–1555.
- Reiss, G., Brueckl, H., Huettner, A., Schotter, J., Brzeska, M., Panhorst, M., Sudfeld, D., Becker, A., Kamp, P.B., Puehler, A., 2005. Magneto-resistive sensors and magnetic nanoparticles for biotechnology. *J. Mater. Res.* 20 (12), 3294–3302.
- Rizzi, G., Lee, J.-R., Guldberg, P., Dufva, M., Wang, S.X., Hansen, M.F., 2017. Denaturation strategies for detection of double stranded PCR products on GMR magnetic biosensor array. *Biosens. Bioelectron.* 93, 155–160.
- Ruan, G., Vieira, G., Henighan, T., Chen, A.R., Thakur, D., Sooryakumar, R., Winter, J.O., 2010. Simultaneous magnetic manipulation and fluorescent tracking of multiple individual hybrid nanostructures. *Nano Lett.* 10 (6), 2220–2224.
- Sagadevan, S., Periasamy, M., 2014. Recent trends in nanobiosensors and their applications—a review. *Rev. Adv. Mater. Sci.* 36, 62–69.
- Sandhu, A., Sanbonsugi, H., Shibasaki, I., Abe, M., Handa, H., 2004. High sensitivity InSb ultra-thin film micro-Hall sensors for bioscreening applications. *Jpn. J. Appl. Phys.* 43 (7A), L868.
- Sandhu, A., Kumagai, Y., Lapicki, A., Sakamoto, S., Abe, M., Handa, H., 2007. High efficiency Hall effect micro-biosensor platform for detection of magnetically labeled biomolecules. *Biosens. Bioelectron.* 22 (9–10), 2115–2120.
- Schneider, M., Hoffmann, H., Zweck, J., 2000. Lorentz microscopy of circular ferromagnetic permalloy nanodisks. *Appl. Phys. Lett.* 77 (18), 2909–2911.
- Schneider, M., Hoffmann, H., Otto, S., Haug, T., Zweck, J., 2002. Stability of magnetic vortices in flat submicron permalloy cylinders. *J. Appl. Phys.* 92 (3), 1466–1472.
- Schneider, M., Liszkowski, J., Rahm, M., Wegscheider, W., Weiss, D., Hoffmann, H., Zweck, J., 2003. Magnetization configurations and hysteresis loops of small permalloy ellipses. *J. Phys. D: Appl. Phys.* 36 (18), 2239–2243.
- Schotter, J., Kamp, P.B., Becker, A., Puhler, A., Brinkmann, D., Schepper, W., Bruckl, H., Reiss, G., 2002. A biochip based on magnetoresistive sensors. *IEEE Trans. Magn.* 38 (5), 3365–3367.
- Schotter, J., Kamp, P.B., Becker, A., Puhler, A., Reiss, G., Bruckl, H., 2004. Comparison of a prototype magnetoresistive biosensor to standard fluorescent DNA detection. *Biosens. Bioelectron.* 19 (10), 1149–1156.
- Schuh, D., Biberger, J., Bauer, A., Breuer, W., Weiss, D., 2001. Hall-magnetometry on ferromagnetic dots and dot arrays. *IEEE Trans. Magn.* 37 (4), 2091–2093.
- Shen, W.F., Liu, X.Y., Mazumdar, D., Xiao, G., 2005. In situ detection of single micron-sized magnetic beads using magnetic tunnel junction sensors. *Appl. Phys. Lett.* 86 (25).
- Tamanaha, C., Mulvaney, S., Rife, J., Whitman, L., 2008. Magnetic labeling, detection, and system integration. *Biosens. Bioelectron.* 24 (1), 1–13.
- Terauchi, N., Noguchi, S., Igarashi, H., Hatsukade, Y., Tanaka, S., 2012. Characteristic analysis of directly coupled HTS dc-SQUID magnetometer with superconducting film magnetic-shield considering Josephson-junction resistance. *IEEE Trans. Magn.* 48 (2), 571–574.
- Terauchi, N., Noguchi, S., Igarashi, H., 2014. Numerical simulation of SQUID magnetometer considering equivalent electrical circuit of Josephson junction. *Phys. Procedia* 58, 200–203.
- Thomson, W., 1856. On the electro-dynamic qualities of metals:—effects of magnetization on the electric conductivity of nickel and of iron. *Proc. R. Soc. Lond.* 8, 546–550.
- Tsukamoto, A., Saitoh, K., Suzuki, D., Sugita, N., Seki, Y., Kandori, A., Tsukada, K., Sugiura, Y., Hamaoka, S., Kuma, H., 2005. Development of multisample biological immunoassay system using HTSSQUID and magnetic nanoparticles. *IEEE Trans. Appl. Supercond.* 15 (2), 656–659.
- Tumanski, S., 2001. *Thin Film Magnetoresistive Sensors*. CRC Press.
- Tumanski, S., 2016. *Handbook of Magnetic Measurements*. CRC Press.
- Vavassori, P., Metlushko, V., Ilic, B., Gobbi, M., Donolato, M., Cantoni, M., Bertacco, R., 2008. Domain wall displacement in Py square ring for single nanometric magnetic bead detection. *Appl. Phys. Lett.* 93 (20), 203502.
- Vieira, G., Henighan, T., Chen, A., Hauser, A.J., Yang, F.Y., Chalmers, J.J., Sooryakumar, R., 2009. Magnetic wire traps and programmable manipulation of biological cells. *Phys. Rev. Lett.* 103, 12.
- Vieira, G., Chen, A., Henighan, T., Lucy, J., Yang, F.Y., Sooryakumar, R., 2012. Transport of magnetic microparticles via tunable stationary magnetic traps in patterned wires. *Phys. Rev. B* 85, 17.
- Wang, S.X., Bae, S.Y., Li, G.X., Sun, S.H., White, R.L., Kemp, J.T., Webb, C.D., 2005. Towards a magnetic microarray for sensitive diagnostics. *J. Magn. Magn. Mater.* 293 (1), 731–736.
- Wang, T., Zhou, Y., Lei, C., Luo, J., Xie, S., Pu, H., 2017. Magnetic impedance biosensor: a review. *Biosens. Bioelectron.* 90, 418–435.
- Williams, E.M., 2001. *Design and Analysis of Magnetoresistive Recording Heads*. J Wiley.
- Wirix-Speetjens, R., Fyen, W., De Boeck, J., Borghs, G., 2006. Single magnetic particle detection: experimental verification of simulated behavior. *J. Appl. Phys.* 99 (10), 103903.
- Xu, J., Li, Q., Zong, W., Zhang, Y., Li, S., 2016. Ultra-wide detectable concentration range of GMR biosensors using Fe<sub>3</sub>O<sub>4</sub> microspheres. *J. Magn. Magn. Mater.* 417, 25–29.
- Yuasa, S., Nagahama, T., Fukushima, A., Suzuki, Y., Ando, K., 2004. Giant room-temperature magnetoresistance in single-crystal Fe/MgO/Fe magnetic tunnel junctions. *Nat. Mater.* 3 (12), 868–871.